# EFFECTIVE STRESS COEFFICIENT OF ROCKS FOR PEAK AND RESIDUAL STRENGTHS

Submitted by

Anjula Buddhika Nayomi Dassanayake

A thesis submitted in partial fulfillment of the requirements for the Degree of Doctor for Philosophy in Engineering

Supervisor: Prof. Yoshiaki FUJII

Rock Mechanics Laboratory

Division of Sustainable Resources Engineering

Graduate School of Engineering

Hokkaido University

September 2015

# EFFECTIVE STRESS COEFFICIENT OF ROCKS FOR PEAK AND RESIDUAL STRENGTHS

Dissertation for the Degree of Doctor of Engineering

A.B.N. Dassanayake
Rock Mechanics Laboratory
Division of Sustainable Resources Engineering
Graduate School of Engineering
Hokkaido University
September 2015

**Acknowledgements**

First and foremost, I wish to express my sincere gratitude to my supervisor Yoshiaki FUJII, Professor, Dr. for his valuable guidance and expert advice, encouragement and constant support that lead to the completion of studies. He was an excellent advisor for me during my stay in graduate school. I would not have been able to precede this far without his patience, insight and plentiful advices. Absolutely he was an integral part of my success, a perfect advisor and I had the good fortune to be one of his students.

I am thankful to Jun-ichi KODAMA, Associate Professor Dr. for his encouragement and suggestions. Heartfelt thanks to Daisuke FUKUDA, Research Associate, Dr. who helped me with X-ray CT. Special thanks to Takayuki SUGAWARA, technician who was very kind to me during the experimental difficulties. I am very much grateful to all my lab mates and friends for their assistance, enduring memories, kindness and great lifetime friendship.

I would like to express my thanks to all the professors of the Division of Sustainable Resources Engineering, Graduate School of Engineering, Hokkaido University for their kind supports.

I am grateful to the Ministry of Education, Culture, Sports and Science and technology, Japan for the doctoral scholarship (MEXT) and the staffs of English Engineering Education Program ($e^3$) for their support.

I thankfully acknowledge the Faculty of Engineering, University of Moratuwa for granting me the study leave to pursue my doctoral studies.

I kindly remind and thank my loving parents, my brother and my sisters for their love, inspirations, patience and constant support in every step of my life. Last but not least, I gratefully acknowledge all the people who gave me support, and help for my studies.

# Effective Stress Coefficient of Rocks for Peak and Residual Strengths

A.B.N. Dassanayake

Rock Mechanics Laboratory

Division of Sustainable Resources Engineering

Graduate School of Engineering

Hokkaido University

## ABSTRACT

To determine the effective stress coefficient for peak and residual strengths ($\alpha_{\text{-Peak}}$ and $\alpha_{\text{-Residual}}$) of rocks, Modified Failure Envelope Method (MFEM) was proposed incorporating the results of both single stage and multistage triaxial compression tests based on the failure envelope method. Multistage triaxial tests are used to reduce the number of specimens as well as the error caused by differences in the mechanical properties between specimens. The effective stress coefficients for intact and fractured rocks ($\alpha_{\text{-Biot's}}$ and $\alpha_{\text{-Fractured}}$) were also evaluated using conventional methods, and the data were compared with the coefficient values obtained by MFEM for the peak and residual strengths.

The types of rock considered were Kimachi sandstone as a medium-hard clastic rock, Bibai sandstone as a hard clastic rock, Inada granite as a hard crystalline rock and Shikotsu welded tuff as a soft pyroclastic rock, to cover a wide range of physical properties of rock under confining pressures of 1-15 MPa at 295 K. Based on the results of rock types, equations to obtain the effective stress coefficient from total confining pressure ($P_c$) or normal stress ($\sigma_n$) and pore pressure, and a method to choose the coefficients for elastic stress analyses and failure evaluations for intact rock structures or structures in rock mass were proposed.

$\alpha_{\text{-Biot's}}$, obtained by conventional hydrostatic compression test method, decreased with increasing confining pressure, and was in the range $1 > \alpha_{\text{-Biot's}} > 0.8$ for Kimachi sandstone and $1 > \alpha_{\text{-Biot's}} > 0.5$ for Bibai sandstone. The effective stress coefficients by hydrostatic tests for fractured rock, $\alpha_{\text{-Fractured}}$ were larger than those for intact rock $\alpha_{\text{-Biot's}}$ and were close to unity for both sandstone types. The effective stress coefficients for the peak strength, $\alpha\text{-}_{\text{Peak}}$ for Kimachi sandstone and Bibai sandstone decreased with increasing effective confining pressure and was in the range $0.8 > \alpha_{\text{-Peak}} > 0.4$ and $0.9 > \alpha_{\text{-Peak}} > 0.4$

respectively under both single and multistage MFEMs. For residual strength, the most reliable $\alpha$-$_{\text{Residual}}$ by multistage MFEM ascending $P_c$ approach was almost same as $\alpha_{\text{-Biot's.}}$

For Inada granite, $\alpha_{\text{-Biot's}}$ decreased with increasing confining pressure and was in the range $0.9 > \alpha_{\text{-Biot's}} > 0.7$. $\alpha_{\text{-Fractured}}$ were larger than those for intact rock $\alpha_{\text{-Biot's}}$ and were close to unity. $\alpha$ value for peak strengths under multistage MFEM decreased with increasing effective confining pressure and were in the range $0.8 > \alpha_{\text{peak}} > 0.2$.

For Shikotsu welded tuff, the effective stress coefficient for intact rock, $\alpha_{\text{-Biot's}}$ slightly decreased with increasing confining pressure and was in the range $0.95 > \alpha_{\text{-Biot's}} > 0.90$. The effective stress coefficients for fractured rock, $\alpha_{\text{-Fractured}}$ were close to unity. The MFEM could not be used to determine the effective stress coefficients for the peak and residual strengths by single stage or multistage triaxial tests. In many cases, the strengths with non-zero pore pressures were larger than that with zero pore pressure. This may be due to an end-cap like failure surface at higher stresses because of pore collapse due to crushing of the rock matrix, which consisted of volcanic glass. Poroelasticity theory could not be applied to this condition.

CONTENTS Page No.

# 1. Introduction

## 1.1 Background

The determination of effective stress is an important aspect of stability analysis, and has a number of engineering applications especially in geotechnical and petroleum engineering, including underground and surface rock structures, oil and gas production, and sequestration of carbon dioxide [Alam et al., 2009; Alam et al., 2010; Hu et al., 2010]. Failure criteria for porous media are represented using the effective stress, the concept of which was first introduced by Terzaghi (1936) for soil, and is commonly known as Terzaghi's effective stress principle. It states that the effect of the total stress $\sigma$ and the pore pressure $P_{\mathrm{p}}$ can be described using a single parameter, which is known as the effective stress $\sigma'$, and is defined as follows:

$$\sigma' = \sigma - P_{\mathrm{p}}. \tag{1.1}$$

In general, Terzarghi's effective stress is not always valid for fluid-related rocks. Therefore, effective stress coefficient was proposed by Biot (1941) to modify the effective stress principle, giving

$$\sigma' = \sigma - \alpha P_{\mathrm{p}}, \tag{1.2}$$

where $\alpha$ is the effective stress coefficient, a key parameter that quantifies the contribution of the pore pressure to the effective stress. For granular soil, the contact area between grains is typically very small; thus, it is possible to assume that a cross section will be occupied mostly by the fluid. For this reason, the corresponding effective stress coefficient can be approximated to $\alpha = 1$. In porous rock with significant cementation, the grain–grain contact will be considerably larger, and it is not possible to assume that the cross section is mostly occupied by the fluid. Consequently the corresponding effective stress coefficient will be less than 1 [Zhang et al., 2009].

Effective stress coefficient is usually calculated using experimentally measured data from the elastic region, based on poroelasticity theory [Biot, 1941, 1955]. Effective stress coefficient values for the peak and residual strengths (Fig. 1.1) are important to evaluate rock failure; however, $\alpha$ obtained as above is not necessarily valid for these strengths. There have been very few investigations into the effective stress coefficient for the peak strength [e.g. Franquet & Abass, 1999], and no investigations of how to determine $\alpha$ for the residual strength of rocks.

## 1.2 Objectives

The objective of this study is to develop an approach to evaluate the effective stress coefficient for peak and residual strengths of rock.

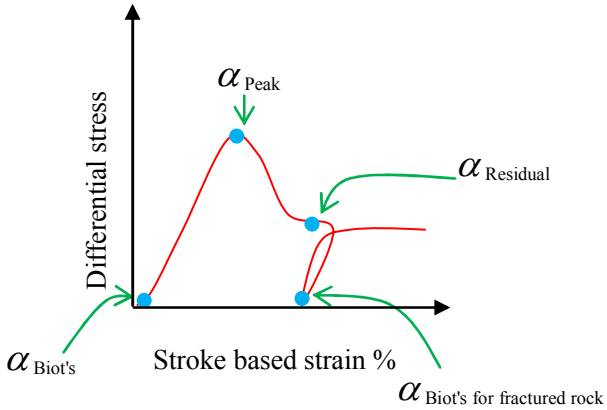


Fig. 1.1 Effective stress coefficient corresponds to different stages of a failure process

## 1.3 Content of the research

In this research, the author proposes Modified Failure Envelope Method (MFEM), incorporating the results of triaxial compression tests to evaluate the effective stress coefficients for the peak and residual strengths of rocks ($\alpha_{\text{-Peak}}$ and $\alpha_{\text{-Residual}}$, Fig. 1.1), based on the failure envelope method proposed by Franquet & Abass (1999).

In the Failure Envelope Method [Franquet & Abass, 1999], they used a tedious trial and error method and an approximation by the linear Coulomb's failure criterion which induces errors during approximation by a straight line to evaluate effective stress coefficient. But in MFEM, the effective stress coefficient can be estimated without a trial and error method or assuming any failure criterion. Moreover, MFEM is the first such study, which considers evaluating effective stress coefficient for residual strength to date.

Multistage triaxial tests are used to reduce the number of specimens as well as the error caused by differences in the mechanical properties between specimens. The effective stress coefficients are also determined using a conventional method under hydrostatic stress states for intact and fractured rocks, and are compared with the values of $\alpha$ for the strengths obtained using the single and multistage MFEMs. Equations to obtain the effective stress coefficient from total confining pressure ($P_c$) or normal stress ($\sigma_n$) and pore pressure, and a method to choose the coefficients for elastic stress analyses and failure evaluations for intact rock structures or structures in rock mass were also proposed.

The types of rock considered were Kimachi sandstone as a medium-hard clastic rock, Bibai sandstone as a hard clastic rock, Inada granite as a hard crystalline rock and Shikotsu welded tuff as a soft pyroclastic rock, to cover a wide range of physical properties of rocks.

In addition, X-ray computed tomography (CT) observation and thin-section image analysis were carried out/referred from Alam et al. (2014) on the specimens after compression. CT images were obtained in three perpendicular planes to determine the macroscopic failure conditions. Microstructure analysis was conducted using thin-section images of specimens that had been impregnated with blue resin.

A maximum effective confining pressure of 15 MPa was established by the maximum capacity of the apparatus. Although this effective confining pressure may not seem sufficiently high, especially for Inada granite, it corresponds to the effective vertical stress at a depth of 882 m and the effective horizontal stress at a depth of 3528 m assuming $\nu$ = 0.2 (Eqs. 1.3 and 1.4). As most underground caverns are constructed to depths of less than 1000 m, this maximum confining pressure value is meaningful.

$$\sigma'_{\mathrm{V}} = \gamma H - P_{\mathrm{p}} \tag{1.3}$$

$$\sigma'_{\mathrm{H}} = \frac{\nu}{1-\nu}\sigma'_{\mathrm{V}} \tag{1.4}$$

where $\sigma'_{\mathrm{v}}$ and $\sigma'_{\mathrm{H}}$ are terzaghi's effective vertical and horizontal stresses (Pa), $\gamma$ is the unit weight (N/m$^3$), $H$ is the depth (m) and $\nu$ is poisson's ratio.

### 1.4 Modified failure envelope method

The MFEM requires the construction of a failure envelope on the differential stress–effective confining pressure plane for saturated samples tested using a triaxial cell with zero pore pressure, followed by that for saturated samples with specific pore pressures (Fig. 1.2). In here, differential stress is the difference between axial stress and confining pressure.

$$\sigma_{\mathrm{d}} = \sigma' - P_{\mathrm{C}}' = \sigma - \alpha P_{\mathrm{p}} - (P_{\mathrm{C}} - \alpha P_{\mathrm{p}}) = \sigma - P_{\mathrm{C}} \tag{1.5}$$

where, $\sigma_{\mathrm{d}}$ is the differential stress (MPa), $\sigma$ is the axial stress (MPa), $P_{\mathrm{c}}$ is the confining pressure (MPa), $\sigma'$ is effective axial stress (MPa), $P_{\mathrm{c}}'$ is effective confining pressure (MPa), $\alpha$ is the effective strength coefficient and $P_{\mathrm{p}}$ is pore pressure (MPa).

Zero pore pressure means pore pressure was controlled to be zero. From the first set of tests with zero pore pressure; Firstly, peak differential stresses are plotted as A ($P_{\mathrm{c}}$=$P_{\mathrm{c1}}$) and B ($P_{\mathrm{c}}$=$P_{\mathrm{c2}}$), as illustrated in Fig. 1.2. For this case, effective confining pressure that equals the total confining pressure.

$$P_{\mathrm{c}}' = P_{\mathrm{c}} \tag{1.6}$$

Secondly, the peak differential stress under $P_c$=$P_{c2}$ from the second set of tests, can be plotted on the differential stress–effective confining pressure plane assuming $\alpha$ = 0 (C in Fig. 1.2) and $\alpha$ = 1 (D in Fig. 1.2). The data with non zero pore pressures can be moved to the left by increasing $\alpha$ from 0 (C) to 1 (D) and the crossing point (E in Fig. 1.2) to the failure envelope for zero pore pressure can be found. For this case,

$$P_c^{'} = P_c - \alpha P_p \tag{1.7}$$

$P_C'$ is the effective confining pressure value at E and $\alpha$ can be determined from $P_C'$ as,

$$\alpha = \frac{P_c - P_c^{'}}{P_p} \tag{1.8}$$

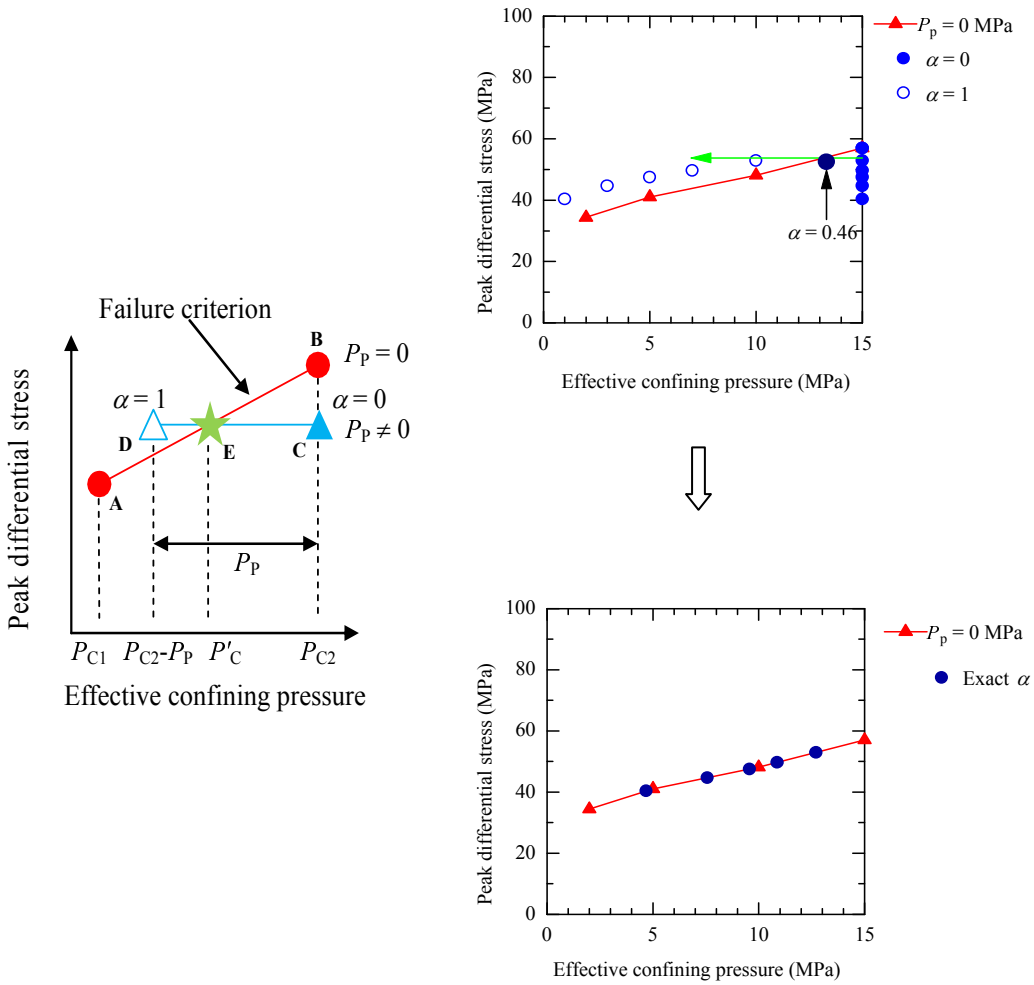


Fig. 1.2 A schematic diagram showing evaluation of $\alpha$ by the modified failure envelope method.

### 1.5 Originality of the research

Many studies have been conducted to determine the Biot's effective stress coefficient using experimentally measured data from the elastic region, based on poroelasticity theory. Effective stress coefficient values for the peak and residual strengths are important to evaluate rock failure; however, $\alpha$ obtained as above is not necessarily valid for these strengths. There have been very few investigations into the effective stress coefficient for the peak strength, and no investigations of how to determine $\alpha$ for the residual strength of rocks. This research is important because it evaluates effective stress coefficient values for the peak and residual strengths. Moreover, MFEM is the first such study, which considers evaluating effective stress coefficient for residual strength to date.

# 2. Experiment on
# Kimachi sandstone

## 2.1 Materials and Method

### 2.1.1 *Specimen and sample preparation*

Kimachi sandstone which was sampled at the Shimane prefecture, Japan was used for the experiments. It is a relatively well-sorted medium-hard clastic rock with a typical grain size in the range 0.4 – 1.0 mm. It consists mostly of rock fragments of andesite and crystal fragments of plagioclase, pyroxene, hornblende, biotite, and quartz, as well as calcium carbonate, iron oxides, and matrix zeolites [Dhakal et al., 2002].

The physical properties of the rock are listed in Table 2.1.

Table 2.1: Physical properties of the Kimachi sandstone shown as "average value (number of specimen) ± standard deviation". UCS: Uniaxial Compressive Strength.

| $V_p$ of specimen (km/s) | $V_s$ of specimen (km/s) | Dry density (g/cm$^3$) | Effective porosity (%) | UCS (saturated) (MPa) |
|---|---|---|---|---|
| 2.24(13) ± 0.08 | 1.478 (13) ± 0.039 | 1.981(13) ± 0.01 | 18.54(13) ± 0.95 | 20.5 (2) ±2.4 |

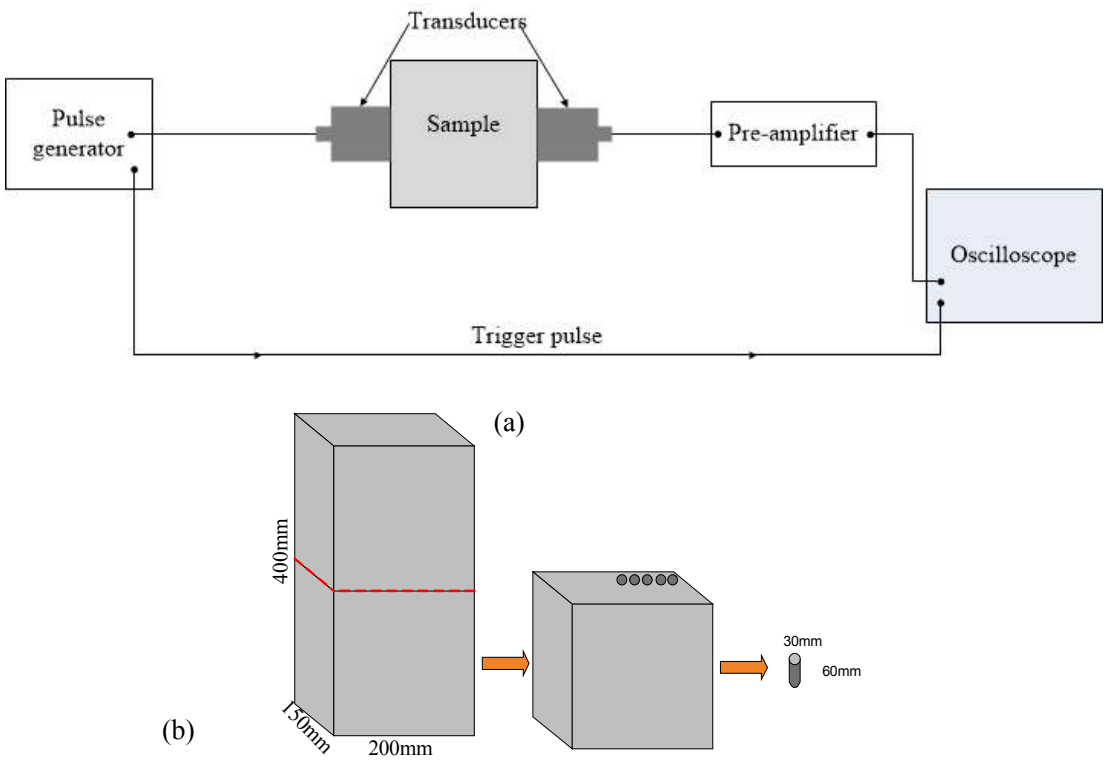


Fig. 2.1 Specimen from block of Kimachi sandstone. (a) Measuring P-wave velocity of the block (b) Specimen after coring, cutting and polishing

The specimens were prepared from a rock block using the following steps; (1) The P-wave velocity along each pair of opposite sides of the rock blocks was measured with 140-kHz sensors (Fig. 2.1). (2) Cylindrical cores with a diameter of 30 mm and a length of 60 mm were prepared in the direction of the slowest P-wave velocity. (3) The core ends were polished to a parallelism of 2/100.

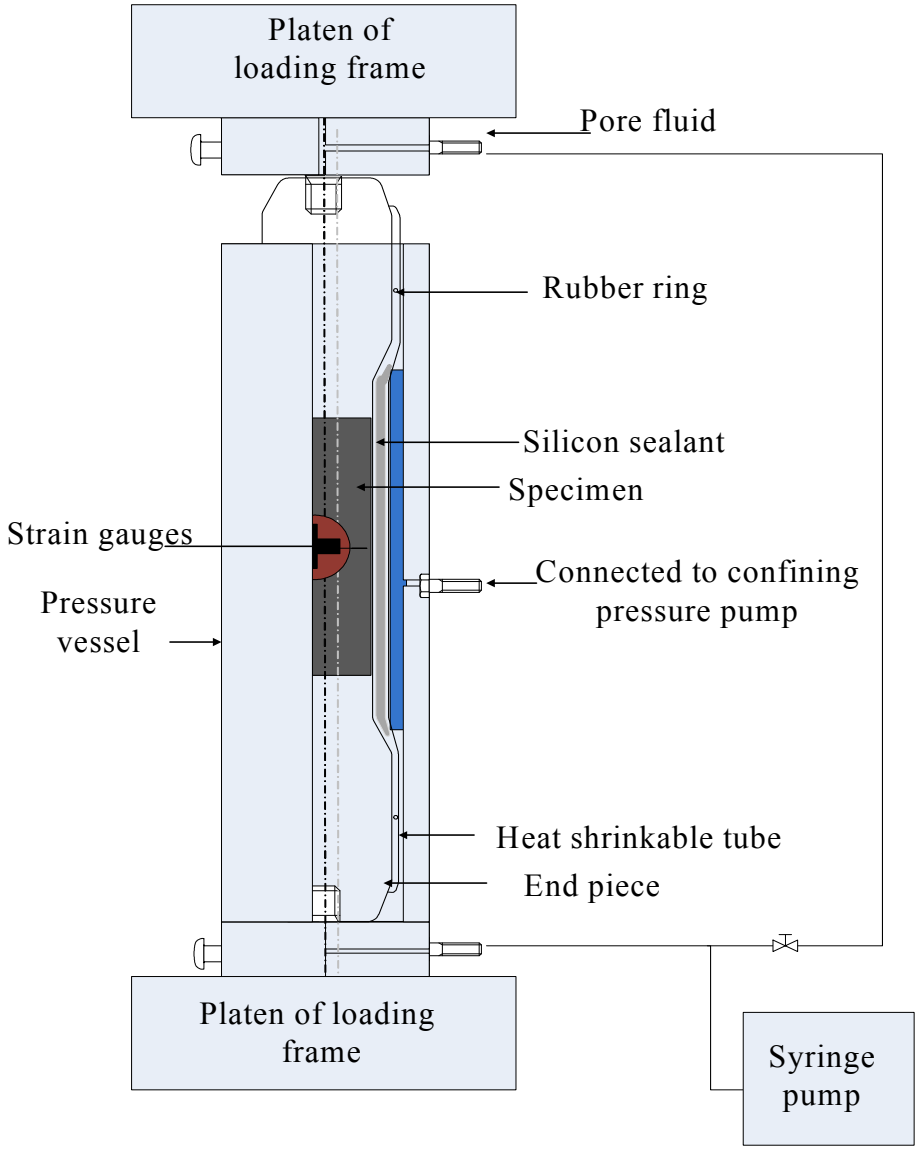


Fig. 2.2 Experimental setup - Pressure vessel with sample and accessories [Dassanayake et al., 2015, 2014]

Table 2.2. Target values of confining pressure and pore pressures for single stage triaxial test

| Confining pressure (MPa) | Pore pressure (MPa) | | | | |
|---|---|---|---|---|---|
| 2 | 0 | 1 | | | |
| 5 | 0 | 1 | 4 | | |
| 10 | 0 | 1 | 4 | 9 | |
| 15 | 0 | 1 | 4 | 9 | 14 |

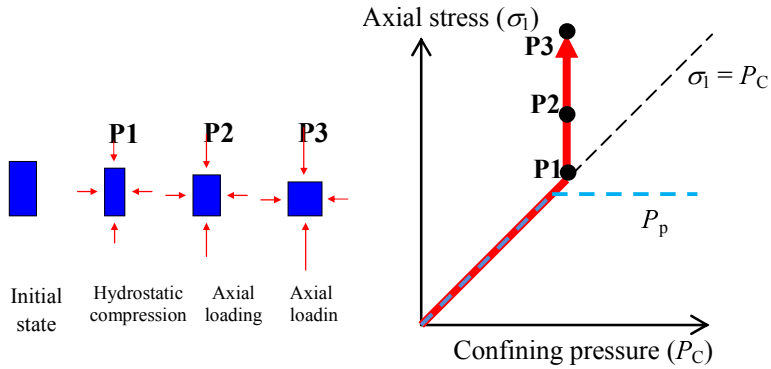


Fig. 2.3. Schematic diagram showing the steps for reaching the desired confining pressure, pore pressure and compression phase of single stage triaxial test. [Dassanayake et al., 2015]

The samples were prepared using the following procedure. (1) Each specimen was made fully pure-water saturated in a water-submergible vacuum jar. (2) Two stainless steel endpieces were attached to a saturated specimen with vinyl tape. The endpieces had a central hole to allow water flow through the specimen. (3) Two cross-type strain gauges were glued to the center of opposite sides of the specimen (only for the case of hydrostatic tests). (4) A coating of silicon sealant was applied to maintain the water flow within the specimen up to the curvature of the endpieces. (5) A heat-shrinkable tube was jacketed to the endpieces-attached specimen to prevent direct contact of the confining fluid (water) with the specimen. (6) The sample was then held in pure water for 24 h.

*2.1.2 Experimental setup*

A loading frame was used to apply the axial load. A double ball plunger pump with a relief valve that was connected to the ultra-compact triaxial cell was used to maintain the confining pressure throughout the experiment. A pair of stainless steel attachments was attached to the jacketed sample. Each attachment had a hole for water flow and a pore pressure sensor. A syringe pump was connected to the lower attachment and used it to control the pore water pressure.

*2.1.3 Experimental procedure*

*2.1.3.1 Single-stage triaxial tests*

The jacketed sample was placed in an ultra-compact triaxial cell [Alam et al., 2014]. After completing the experimental set up as shown in Fig. 2.2, the axial stress, confining pressure, and pore pressure were incremented to the target values listed in Table 2.2 (Fig. 2.3). After reaching the target confining pressure, and pore pressure, they were maintained constant and a constant strain rate ($10^{-5}$ $s^{-1}$, i.e., 0.036 mm/min)-controlled compression was applied until the stroke-based strain reached 5% (3 mm). The effect of temperature on effective stress coefficient should be considered in future. However, the effect has not been considered in the present work and all the tests have been conducted at 295 K. During the experiment, the load, stroke, pore pressure, and confining pressure were measured at a sampling interval of 1 s.

*2.1.3.2 Multistage triaxial tests*

In the multistage triaxial tests, only two samples were required. One sample was tested with zero pore pressure (Sample #1 in Fig. 2.5) using a modified multistage triaxial test [Youn and Tonon, 2010], which is a modification of the ISRM method [Kovari et al., 1983]. The confining pressure was first increased up to the first target value (2 MPa), and an axial compression was introduced at a constant axial strain rate of $10^{-5}$ $s^{-1}$ (0.036 mm/min) until the sample reached the first failure point. Following this, the differential stress was released completely [Youn and Tonon, 2010] and the confining pressure was hydrostatically increased to the next level, 5 MPa, as shown in Fig. 2.4a. The differential stress was then increased to the second failure point, and so on. The failure point was defined by the region of the stress–axial strain curve where the tangent modulus becomes zero [Youn and Tonon, 2010]. The confining pressure was increased stepwise

to 2 MPa, 5 MPa, 10 MPa, and 15 MPa.

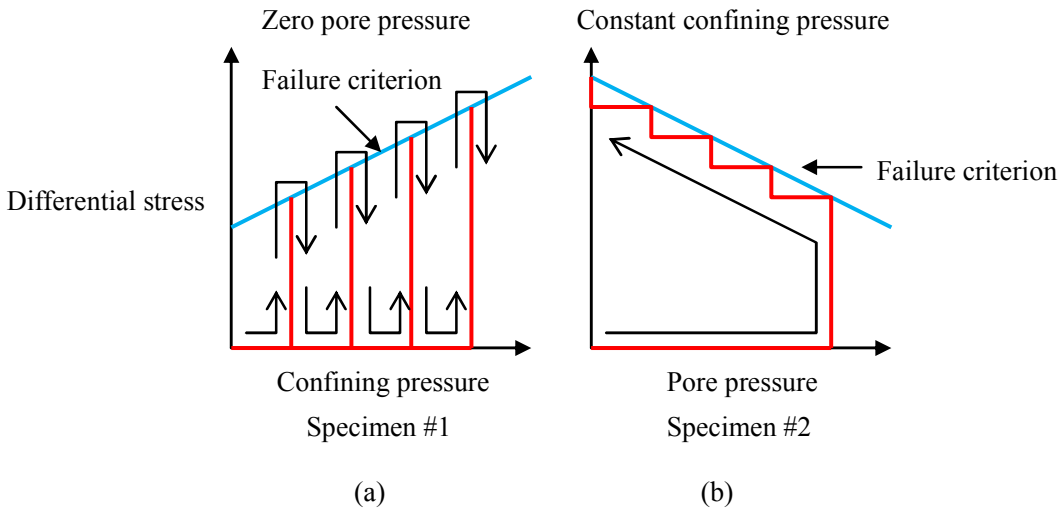


Fig. 2.4 (a) Schematic diagram showing the steps for reaching the desired confining pressure, and compression phase of multi-stage triaxial test- with zero pore pressure. (b) Schematic diagram showing the steps for reaching the desired pore pressure and compression phase while maintaining a constant confining pressure, of multi-stage triaxial test- with pore pressure [Dassanayake et al., 2015].

The second sample was tested by applying a non-zero pore pressure (Sample #2 in Fig. 2.5). In this test, the confining pressure and the pore pressure were introduced successively up to the first target values (15 MPa and 14 MPa, respectively). Axial compression was then introduced at the same strain rate until it reached the first failure point. The pore pressure was then reduced to the next level while maintaining a constant confining pressure of 15 MPa, and axial stress was introduced until the second failure point was reached, as shown in Fig. 2.4b. This procedure was repeated in 6 steps as the pore pressure was reduced to 12 MPa, 10 MPa, 8 MPa, 5 MPa, 1 MPa, and 0 MPa (see Table 2.3).

Due to the heterogeneity of samples, if Sample #2 is weaker than Sample #1 (Fig. 2.5a) $\alpha$ could not be obtained or could be overestimated. If Sample #2 is stronger than Sample #1 (Fig. 2.5b) $\alpha$ could be underestimated. Hence, prior to plotting the peak differential stresses for the Sample #2 ($PDS_2$), the stresses were corrected to reduce the variation in strength between specimens according to Eq. 2.1.

$$PDS_2' = \frac{PDS_1^0}{PDS_2^0} \times PDS_2 \,, \tag{2.1}$$

where $PDS_i^0$ is the peak differential stress of Specimen #$i$ under zero pore pressure (#$i$, $P_p = 0$ in Fig. 2.5).

Table 2.3. Target values of confining pressure and pore pressures for multistage test with non zero pore pressure.

| Confining pressure (MPa) | Pore pressure (MPa) |
|---|---|
| 15 | 14 |
| 15 | 12 |
| 15 | 10 |
| 15 | 8 |
| 15 | 5 |
| 15 | 1 |
| 15 | 0 |

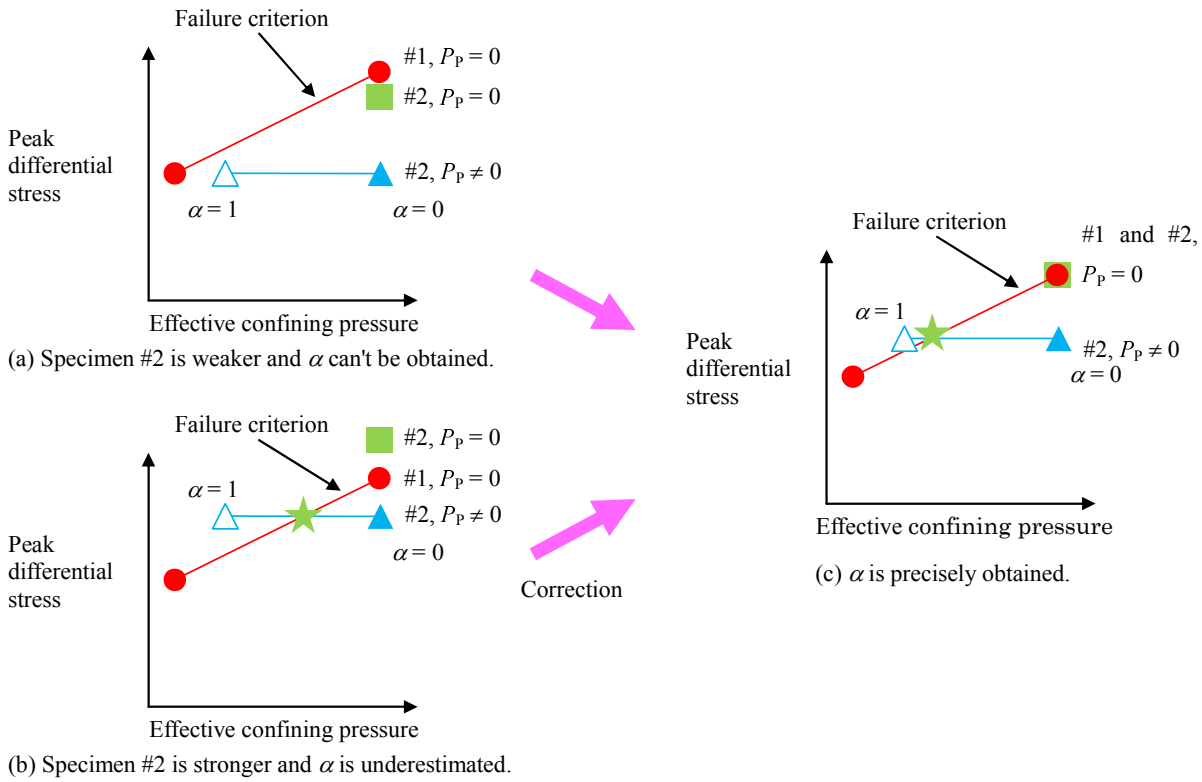


Fig. 2.5 Correction of the peak differential stress for multistage tests [Dassanayake et al., 2015].

Reducing the pore pressure to 0 MPa is important to enable this correction.

*2.1.3.3 Multistage triaxial tests to determine* $\alpha_{\text{-Residual}}$ (Descending $P_c$ method)

Two testing approaches were used to determine $\alpha_{\text{-Residual}}$, using multistage triaxial compression test. Only two samples were required for each approach.

In the first approach, 1st sample was tested with zero pore pressure. The confining pressure was first increased up to the first target value (15MPa), and an axial compression was introduced at a constant axial strain rate of $10^{-5}$ $s^{-1}$ (0.036 mm/min) until the sample reached the residual stress state. Following this, the confining pressure was reduced to 10 MPa and allowed it to reach its residual stress level. This procedure was repeated for 5 MPa and 2 MPa confining pressures (Fig. 2.6).

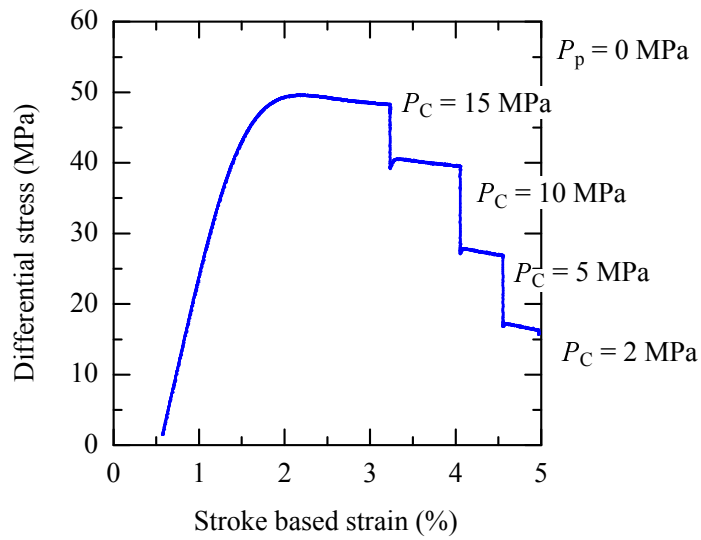


Fig. 2.6 Differential stress versus stoke based strain graph for the sample tested *Multistage triaxial tests* -Descending $P_c$ method with zero pore pressure

Second sample was tested by applying none zero pore pressure. In this test, the confining pressure and the pore pressure were introduced successively up to the first target values; 15 MPa and 0 MPa, respectively. Axial compression was then introduced at the same strain rate until it reached the residual stress state.

The pore pressure was then increased to the next level while maintaining a constant confining pressure of 15 MPa. This procedure was repeated by increasing pore pressure to 3 MPa, 5 MPa, 8 MPa, 10 MPa and

14 MPa (Fig. 2.7). In this approach, effective confining pressure was reduced stepwise and hence this method was named as descending confining pressure method.

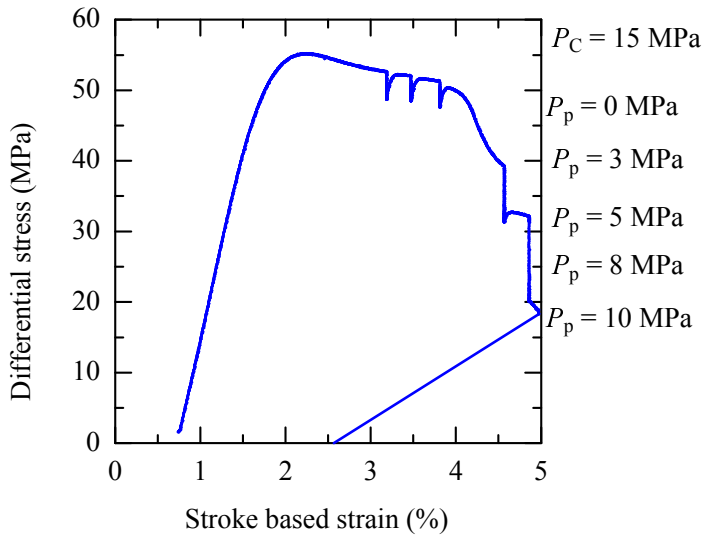


Fig. 2.7 Differential stress versus stoke based strain graph for the sample tested *Multistage triaxial tests* -Descending $P_c$ method with non zero pore pressure

*2.1.3.4 Multistage triaxial tests to determine* $\alpha_{\text{-Residual}}$ (Ascending $P_c$ method)

In the second approach, 1st sample was tested with zero pore pressure as in the 1st approach. The confining pressure was applied in an ascending order starting from 2 MPa, and an axial compression was introduced at a constant axial strain rate of $10^{-5}$ $s^{-1}$ (0.036 mm/min) until the sample reached the residual stress state. Following this, the confining pressure was increased to 5 MPa and allowed it to reach its residual stress level. This procedure was repeated for10 MPa and 15 MPa confining pressures (Fig. 2.8).

Second sample was tested by applying none zero pore pressure. In this test, the confining pressure and the pore pressure were introduced successively up to the first target values; 15 MPa and 14 MPa, respectively. Axial compression was then introduced at the same strain rate until it reached the residual stress state. The pore pressure was then decreased to the next level while maintaining a constant confining pressure of 15 MPa. This procedure was repeated by increasing pore pressure to 10 MPa, 8 MPa, 5 MPa, 3 MPa and 0 MPa (Fig. 2.9). In this approach, effective confining pressure was increased stepwise and hence this method was named as ascending confining pressure method.

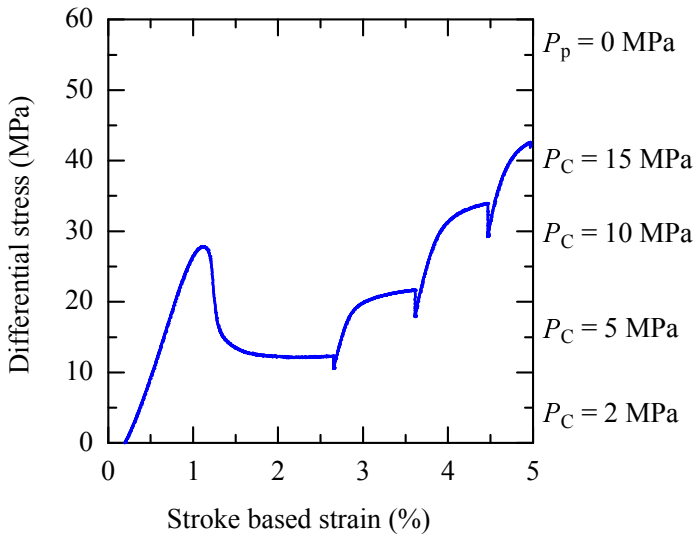


Fig. 2.8 Differential stress versus stoke based strain graph for the sample tested *Multistage triaxial tests* -Ascending $P_c$ method with zero pore pressure

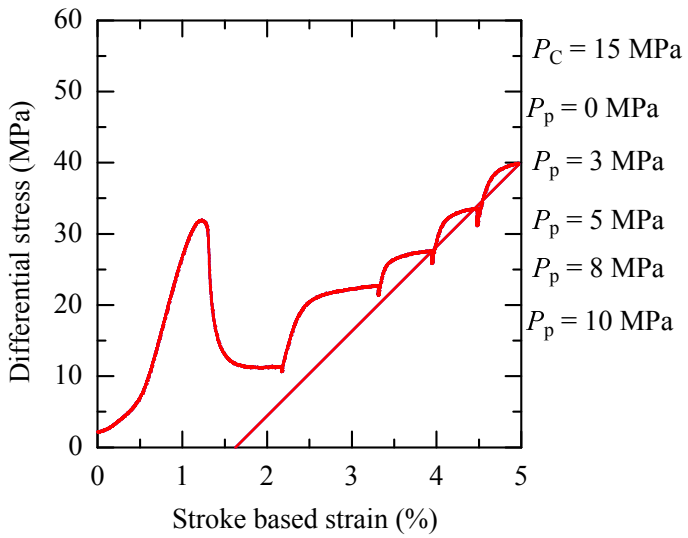


Fig. 2.9 Differential stress versus stoke based strain graph for the sample tested *Multistage triaxial tests* -Ascending $P_c$ method with non zero pore pressure

*2.1.3.5 Hydrostatic tests for intact rock to evaluate* $\alpha$-$_{\text{Biot's}}$

In the hydrostatic tests, specimens were exposed to an increased stress state with an isotropic stress field. Two tests were required: one to determine the bulk modulus of the rock, $K$, as a function of hydrostatic stress, and the other to determine the bulk modulus of the solid matrix (*i.e.*, mineral grains), $K_s$ [Detournay and Cheng, 1993; Hu et al., 2010; Zimmerman, 1991].

The sample preparation process followed the same procedure as detailed in section 2.1.1, except that in the hydrostatic tests, two cross-type strain gauges were attached to the specimen to measure the axial and lateral strains. The bulk modulus of rock, $K$ was evaluated using a drained hydrostatic compression test [Detournay and Cheng, 1993; Hu et al., 2010; Zimmerman, 1991]. In this test, the hydrostatic stress was incremented up to 15 MPa under drained condition and with zero pore pressure to determine $K$, as shown in Fig. 2.10a.

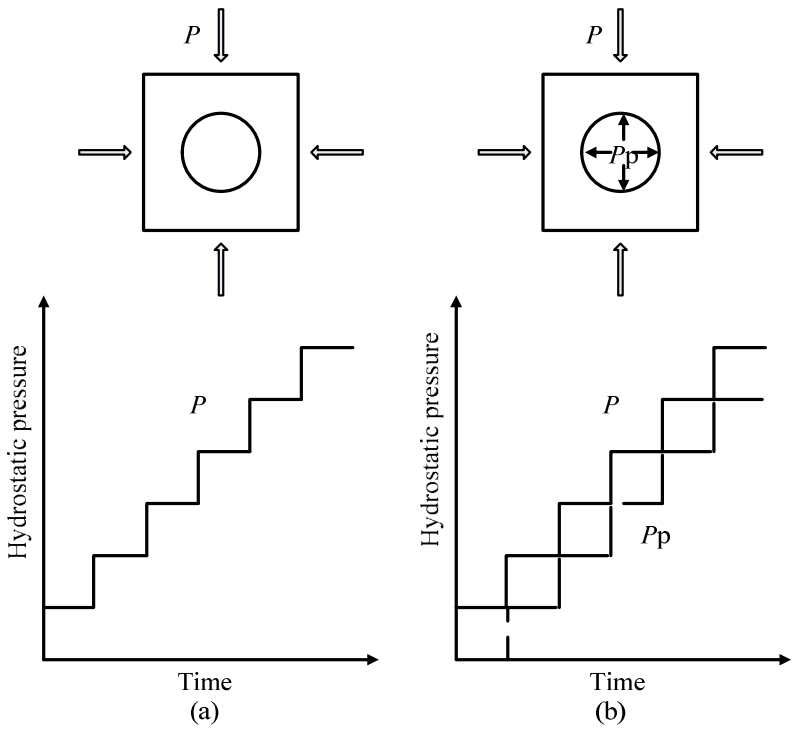


Fig. 2.10 Stress paths of hydrostatic compression tests (a) with zero pore pressure: $P_p$= 0. (b) with non-zero pore pressure: $\Delta P_c = \Delta P_p$.

The volumetric strain was calculated from the axial strain $\varepsilon_a$ and the lateral strain $\varepsilon_l$ using $\varepsilon_v = \varepsilon_a + 2\varepsilon_l$. The bulk modulus was calculated from the volumetric strain curve as a function of the hydrostatic stress

(Fig. 2.11) using the following relation:

$$K = \left( \frac{\Delta P}{\Delta \varepsilon_{\mathrm{v}}} \right)_{\Delta P_{\mathrm{p}}=0} \tag{2.2}$$

where $\Delta P$ is the hydrostatic stress increment, $\Delta \varepsilon_{\mathrm{v}}$ is the volumetric strain increment, and $\Delta P_{\mathrm{p}}$ is the pore pressure increment.

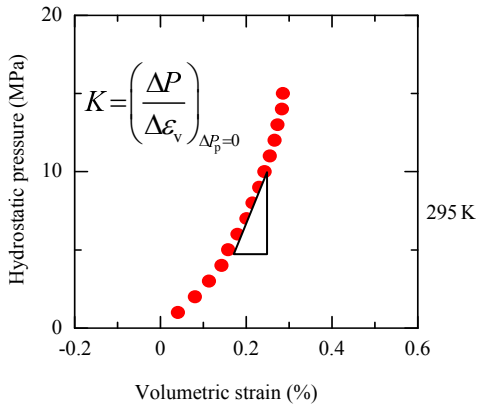


Fig. 2.11 Stress-strain curve in hydrostatic compression test for $P_{\mathrm{p}} = 0$.

In the second hydrostatic test, the hydrostatic stress and pore pressure were simultaneously incremented up to 15 MPa using the same increments (*i.e.*, $\Delta P = \Delta P_{\mathrm{p}}$), and maintaining $P_{\mathrm{p}} = P - 1$ (MPa), as shown in Fig. 2.10b, to determine the bulk modulus of the solid matrix, $K_{\mathrm{s}}$ [Detournay and Cheng, 1993; Hu et al., 2010]. After determining the volumetric strain, $K_{\mathrm{s}}$ was calculated from the linear region of the volumetric strain curve (Fig. 2.12) by,

$$K_{\mathrm{s}} = \left( \frac{\Delta P}{\Delta \varepsilon_{\mathrm{v}}} \right)_{\Delta P_{\mathrm{p}}=\Delta P} \tag{2.3}$$

The initial part of the curve is not linear. This could be due to lack of contact between the strain gages and the specimen under small hydrostatic pressure.

According to the relationship between Biot's coefficient and the compressibility properties [Biot, and

Willis, 1957; Detournay and Cheng, 1993; Geertsma, 1957; Makhnenko and Labuz, 2013; Nur and Byerlee, 1971], Biot's coefficient can be determined by,

$$\alpha_{\text{-Biot's}} = 1 - \frac{K}{K_s} \tag{2.4}$$

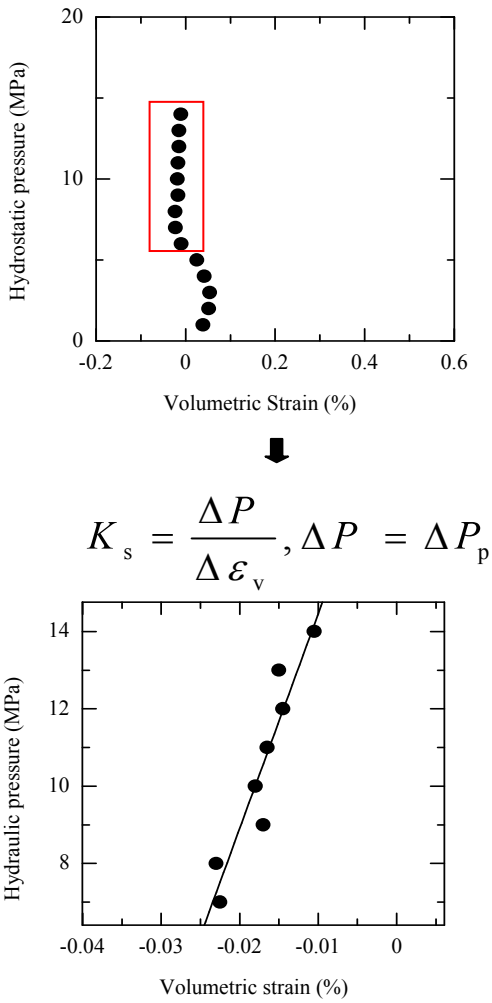


Fig. 2.12 Stress-strain curve in hydrostatic compression test with non zero pore pressure: $\Delta P = \Delta P_p$

*3.1.3.6 Hydrostatic tests for fractured rock to evaluate* $\alpha$-$_{\text{Fractured}}$

Bulk modulus of solid matrix, $K_s$ was measured in advance for intact rock specimen. To evaluate the effective stress coefficient for fractured rock, the bulk modulus of fractured rock must be determined.

Fractured rock specimens were produced from intact rock samples after fracturing them in standard triaxial compression tests with a confining pressure of 2 MPa and a pore pressure of 1 MPa. When the sample reached its residual state, the axial loading was terminated and the differential stress was released

completely. The hydrostatic stress was then incremented up to 15 MPa under drained conditions with a constant pore pressure of 1 MPa to determine the bulk modulus of the fractured rock, $K_f$, as a function of the hydrostatic stress. The increment in the volumetric strain is given by,

$$\Delta\varepsilon_v = \frac{\Delta V}{V} + \frac{\Delta P}{K_s} \tag{2.5}$$

where $\Delta V$ is the water drainage increment and $V$ is the volume of the specimen. The bulk modulus of the fractured rock and $\alpha$-$_{\text{Fractured}}$ are given by,

$$K_f = \left(\frac{\Delta P}{\Delta\varepsilon_v}\right)_{P_p\text{-constant}} . \tag{2.6}$$

$$\alpha_{\text{-Fractured}} = 1 - \frac{K_f}{K_s} \tag{2.7}$$

*2.1.4 Micro- and macrostructure analysis*

Microstructure analysis was conducted from thin-section images of the blue resin-impregnated specimens using ImageJ, public domain open source software [Schneider et al 2012; Schindelin et al 2012 ] with a resolution of 8.8 μm. A micro-focus X-ray computed tomography (CT) scanner, installed at Hokkaido University, Japan, was also used to determine the number, orientation, and geometry of the rupture planes (i.e., the post-compression macrostructure of the specimens). A detailed description of micro-focus X-ray CT for rock-like materials is provided in [Fukuda et al., 2012]. The CT images were obtained in three perpendicular planes with a resolution of 37 μm.

## 2.2 Results

*2.2.1 Deformation of rocks*

It was confirmed that either peak or residual strength increased with increasing confining pressure and decreased with increasing pore pressure (Fig. 2.13). There is no obvious difference between the strengths obtained by single (Fig. 2.13a) and multistage (Fig. 2.13c) triaxial test. A transition from typical brittle to ductile behavior was clearly observed as the confining pressure increased, as shown in Figs 2.14 and 2.15a. The inverse happens when introducing pore pressure. There was a transition from ductile to brittle behavior as pore pressure increased (Fig. 2.15b).

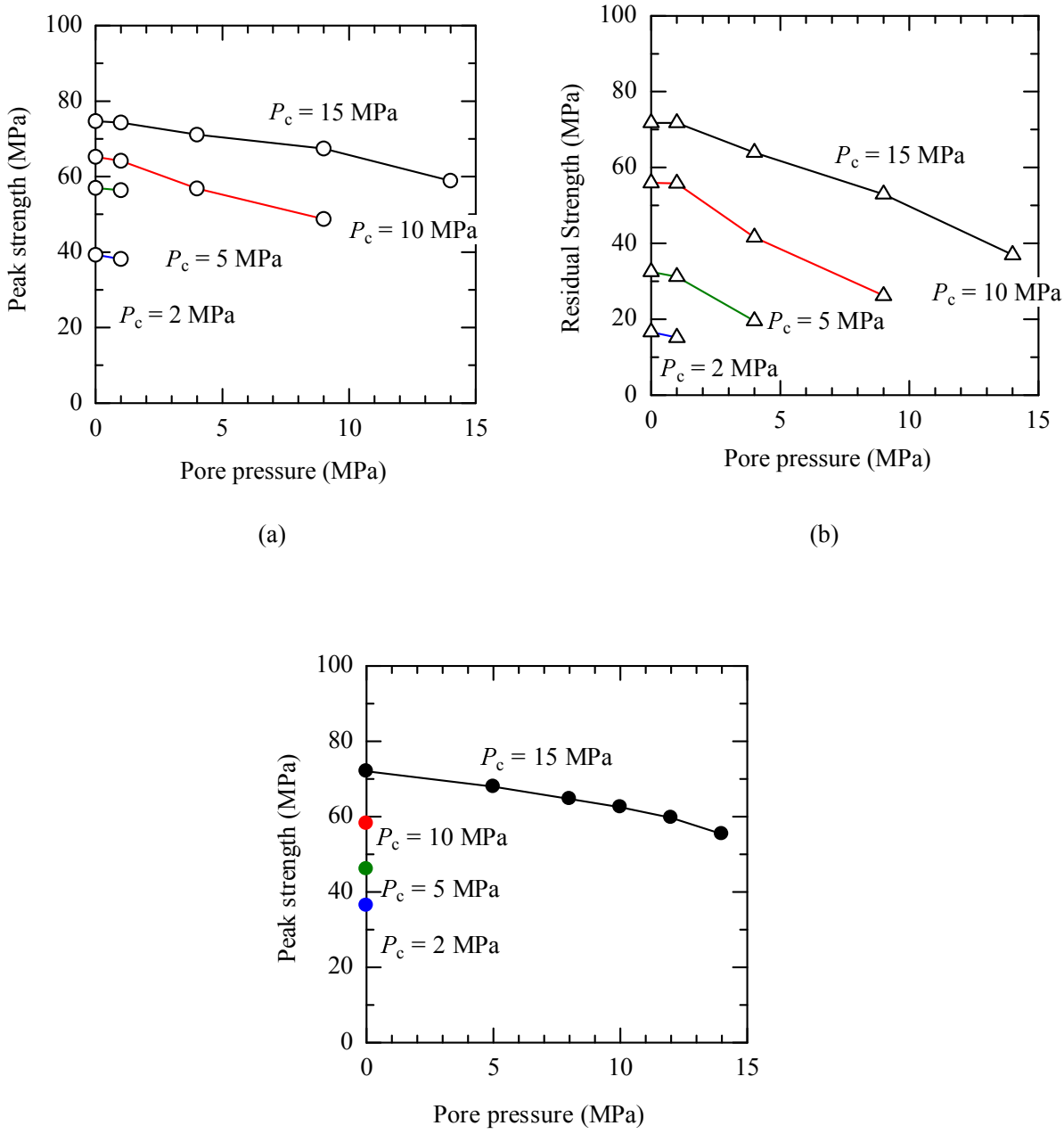


Fig. 2.13 (a) Peak strength with pore pressure for different confining pressures. (b) Residual strength with pore pressure for different confining pressures for single stage triaxial tests. (c) Peak strength with pore pressure for multistage triaxial test.

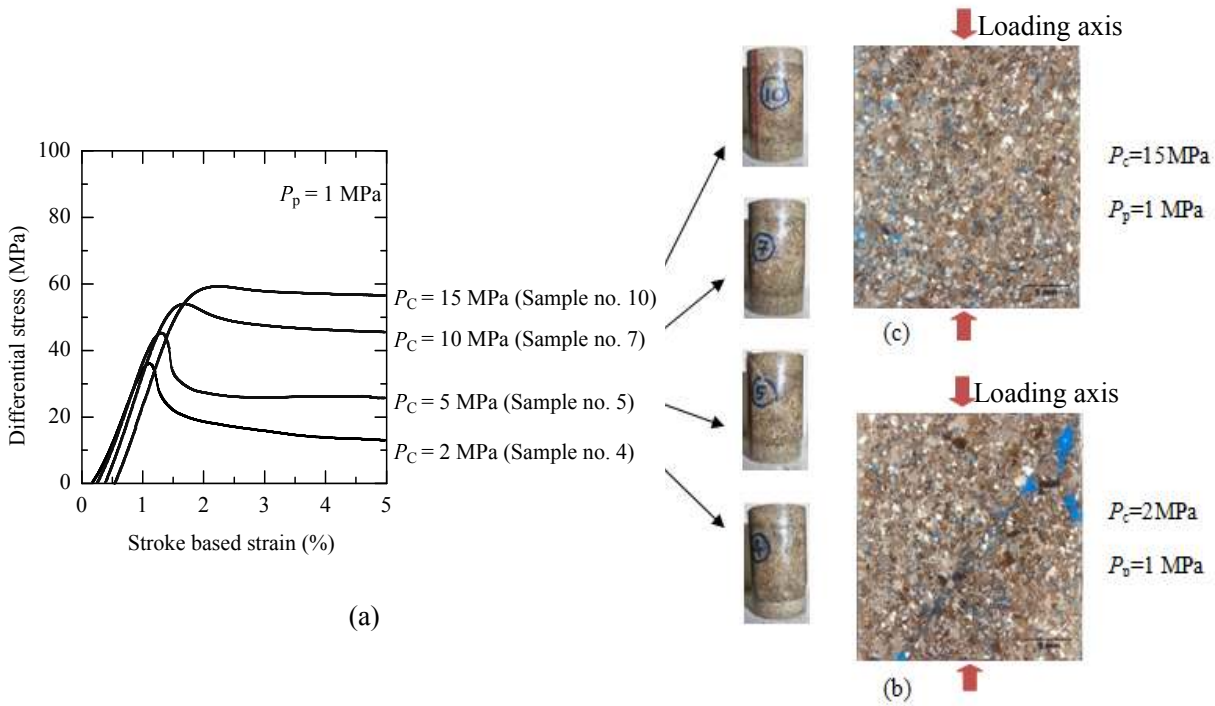


Fig. 2.14 Deformation of Kimachi sandstone samples tested in triaxial compression cell with confining pressure (a) Differential stress versus stoke based strain graph and blue resin-impregnated thin-section images for (b) 2 MPa confining pressure and 1 MPa pore pressure and (c) 15 MPa confining pressure and 1 MPa pore pressure.

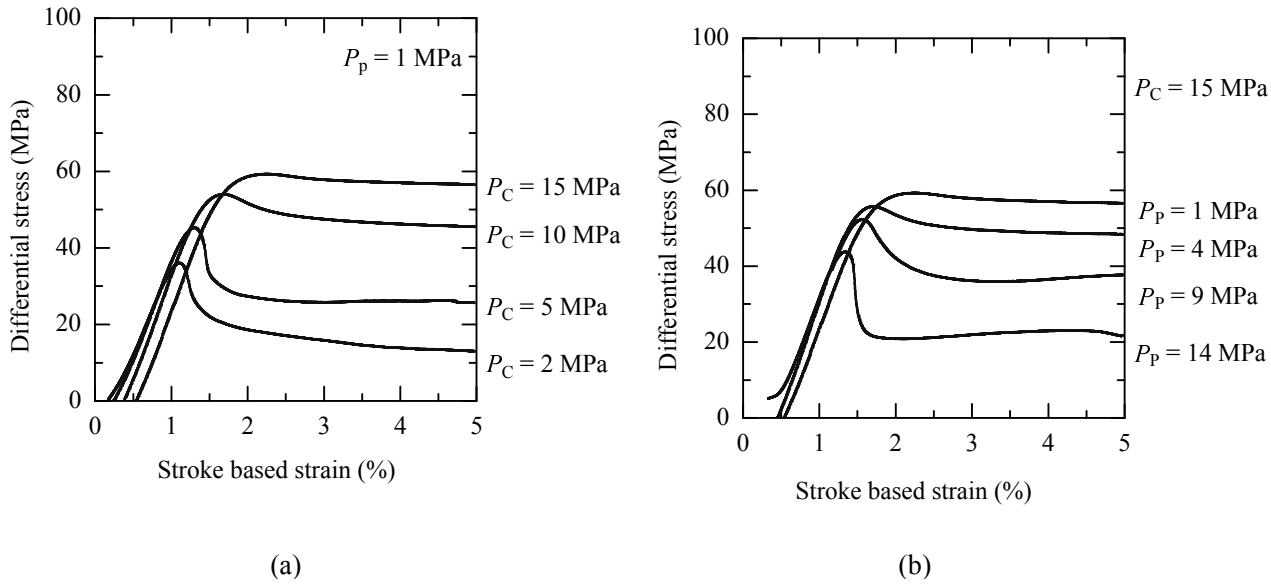


Fig. 2.15 Differential stress versus stoke based strain for different confining pressures and pore pressures. (a) Effect of confining pressure (b) Effect of pore pressure.

With small confining pressures of 2 MPa and 5 MPa, the rock exhibited a nonlinear stress–strain relation at the initial stage of the stress–strain curve (see Fig. 2.15a), which is attributed to the closure or compaction of elliptical pores and pre-existing cracks [Sheng et al., 2012]. However, at higher confining pressures of 10 MPa and 15 MPa, the phase corresponding to microcrack closure at the initial stage of the stress–strain curve was not distinct, which suggests that the closure already occurred before axial loading under the high confining pressures. Following the closure phase, all the specimens deformed elastically. The departure from linear behavior was marked as the yield point (see Fig. 2.15a). The amount of the magnitude of permanent set, which is the phase in-between the maximum strength and yielding point, was increased with increasing confining pressure although it remains small.

With low confining pressures of 2 MPa and 5 MPa, the Kimachi sandstone exhibited strain softening with clustering of localized shear damage (see Fig. 2.14). In contrast, at higher confining pressures of 10 MPa and 15 MPa, the rock exhibited strain hardening with compactive cataclastic flow (see Fig. 2.14). In other words, at lower effective confining pressures ($P_c$ = 2 MPa and 5 MPa with $P_p$ = 1 MPa) only a single rupture plane formed in the Kimachi sandstone (Fig. 2.14b). Almost perfectly elasto-plastic deformation was observed in the Kimachi sandstone under high effective confining pressure and rupture plane was absent (Fig. 2.14c). This occurred because large plastic deformation took place in the cementing materials.

Residual differential stresses obtained by descending $P_c$ approach (Figs. 2.6 and 2.7) of multistage triaxial tests are higher than ascending $P_c$ approach (Figs. 2.8 and 2.9). In descending $P_c$ approach the first step of multistage test was done under a higher effective confining pressure ($P_c$ = 15 MPa and $P_p$ = 0 MPa). Hence sample was subjected to a strain hardening with compactive cataclastic flow. But, in ascending $P_c$ approach, the first step of multistage test was done under a low effective confining pressure ($P_c$ = 15 MPa and $P_p$ = 14 MPa) which exhibited strain softening with clustering of localized shear damage in the first step. This is the reason for the variation of residual differential stresses obtained by these two approaches.

### *2.2.2 Micro- and macrostructures*

From the blue resin-impregnated thin-section analysis, the average thickness of cementing materials of the specimens after axial compression of Kimachi sandstone at 2 MPa was much thicker than the average thickness at 15 MPa (Fig. 2.16).

From the CT observations conducted by Alam et al (2014), a distinct main rupture plane was observed in the X−Z plane of the specimen after axial compression at $P_c$ = 1 MPa (Fig. 2.17a). Several subrupture

planes were discovered in the Y−Z and X−Y planes (Fig. 2.17b) and the average thickness of cementing materials was 0.27 mm under this confining pressure. At $P_c$ = 7 MPa, only one main rupture plane was found in the X−Z and Y−Z planes (Fig. 2.17b). At 15 MPa, no macroscopic rupture planes were observed in either the CT images (Fig. 2.17c) or the blue resin-impregnated thin section (Fig. 2.17e). Under this confining pressure the thickness of the cementing materials was 0.20 mm.

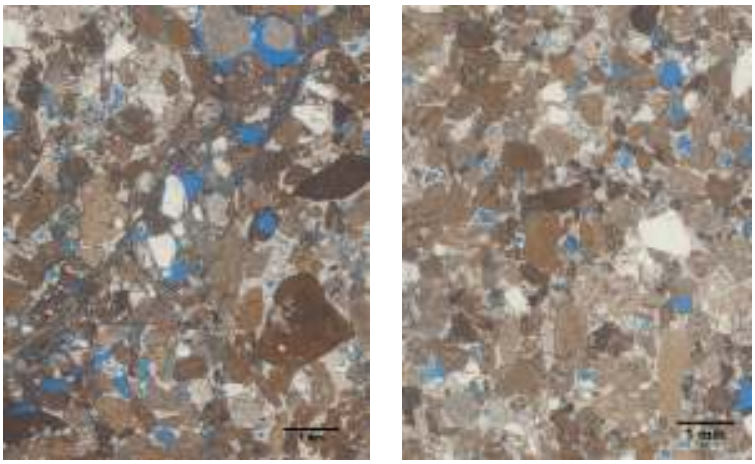

$P_c$=2 MPa, $P_p$ = 1 MPa　　$P_c$=15 MPa, $P_p$ = 1 MPa

Fig. 2.16 Blue resin-impregnated thin-section images and analysis of the specimen after compression with the Kimachi sandstone under $P_c$ = 2 MPa and 15 MPa with $P_p$ = 1 MPa.

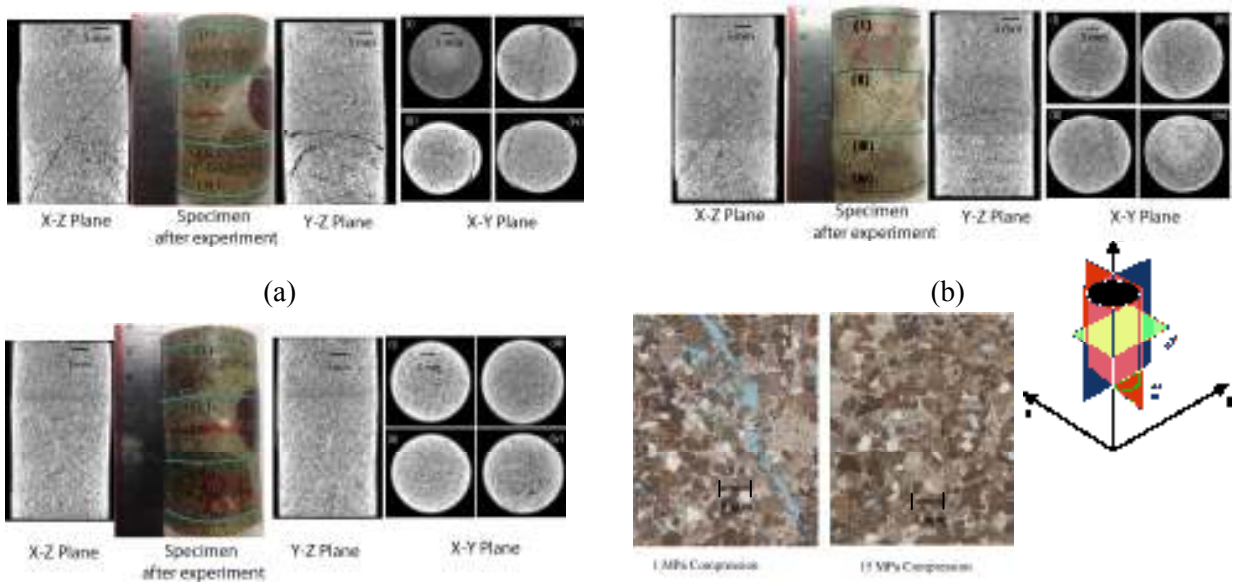


Fig. 2.17 Specimen, CT images, and blue resin-impregnated thin-section images of the specimens after axial compression of Kimachi sandstone. Specimen and CT images at (a) 1 MPa, (b) 7 MPa, and (c) 15 MPa. Blue resin-impregnated thin-section image at (d) 1 MPa and (e) 15 MPa. The loading direction is vertical. [Alam et al., 2014, 2013]

*2.2.3 Effective stress coefficients*

*2.2.3.1 Effective stress coefficients by MFEM*

Effective stress coefficients for peak and residual strengths were obtained from peak differential stress and differential stress in the residual strength state, respectively (Fig. 2.18) through MFEM. In this analysis, stress data related to 1 MPa pore pressure were omitted as the small $P_p$ magnitude caused large errors in $\alpha$ value. When consider about the effective stress coefficient for strength, Jaeger et al. (2007) stated that effective stress coefficient for strength was unity. However, in our experiments, the effective stress coefficients for the peak strength, $\alpha_{\text{-Peak}}$ decreased with increasing effective confining pressure and was in the range $0.8 > \alpha_{\text{-Peak}} > 0.4$, under both single and multi stage MFEMs, as shown in Fig. 2.20.

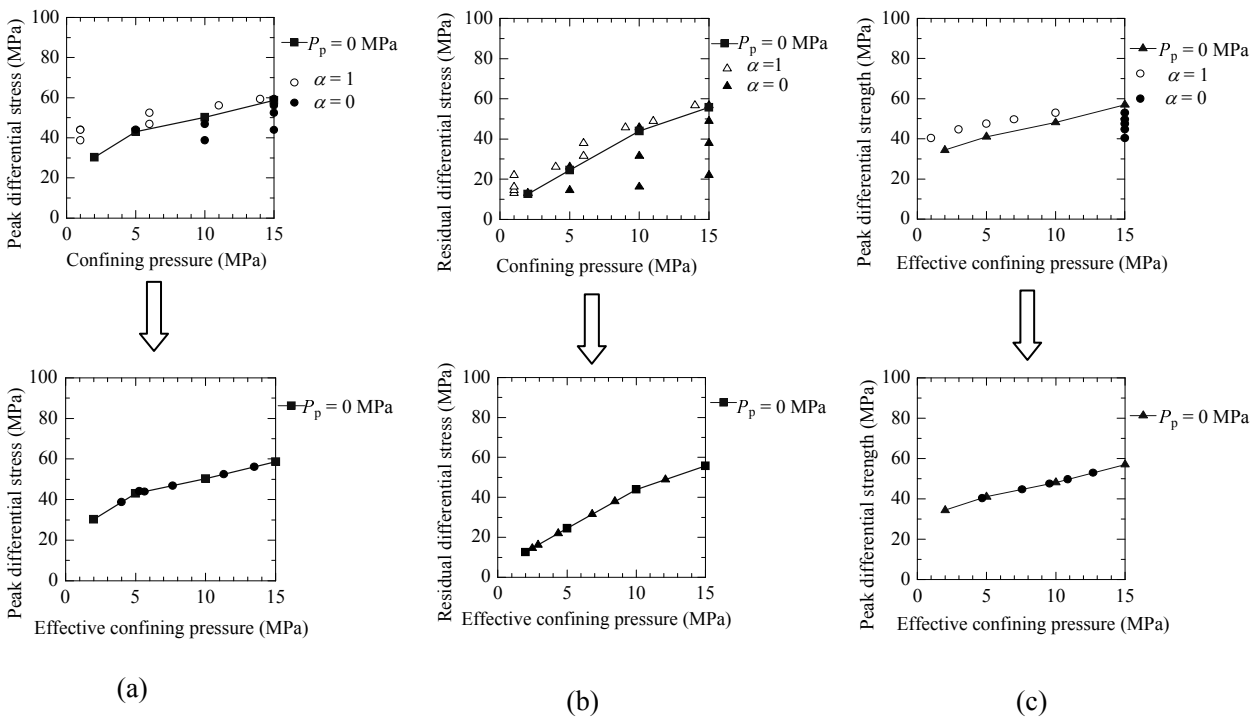


Fig. 2.18 a) Peak differential stresses in single stage MFEM b) Residual differential stresses in single stage MFEM and c) Peak differential stresses multistage MFEM

It is considered that the increased axial stress with confining pressure increased the grain to grain contact area and hence effective stress coefficient increased with increasing effective confining pressure.

For residual strength, $\alpha$-$_{Residual}$ was almost constant under single stage MFEM (Fig. 2.20). But it shows slight decrease with increasing effective confining pressure in both approaches of multistage MFEM (Fig 2.19). In Multistage MFEM-Descending *P*c approach, stress data related to small $P_p$ magnitude; 3 MPa and 5 MPa caused large errors in $\alpha$ value (Fig 2.19). Compaction effect of sample under multistage descending *P*c approach could also cause to this larger deviate of $\alpha$ from constant trend under higher $P_p$ magnitudes.

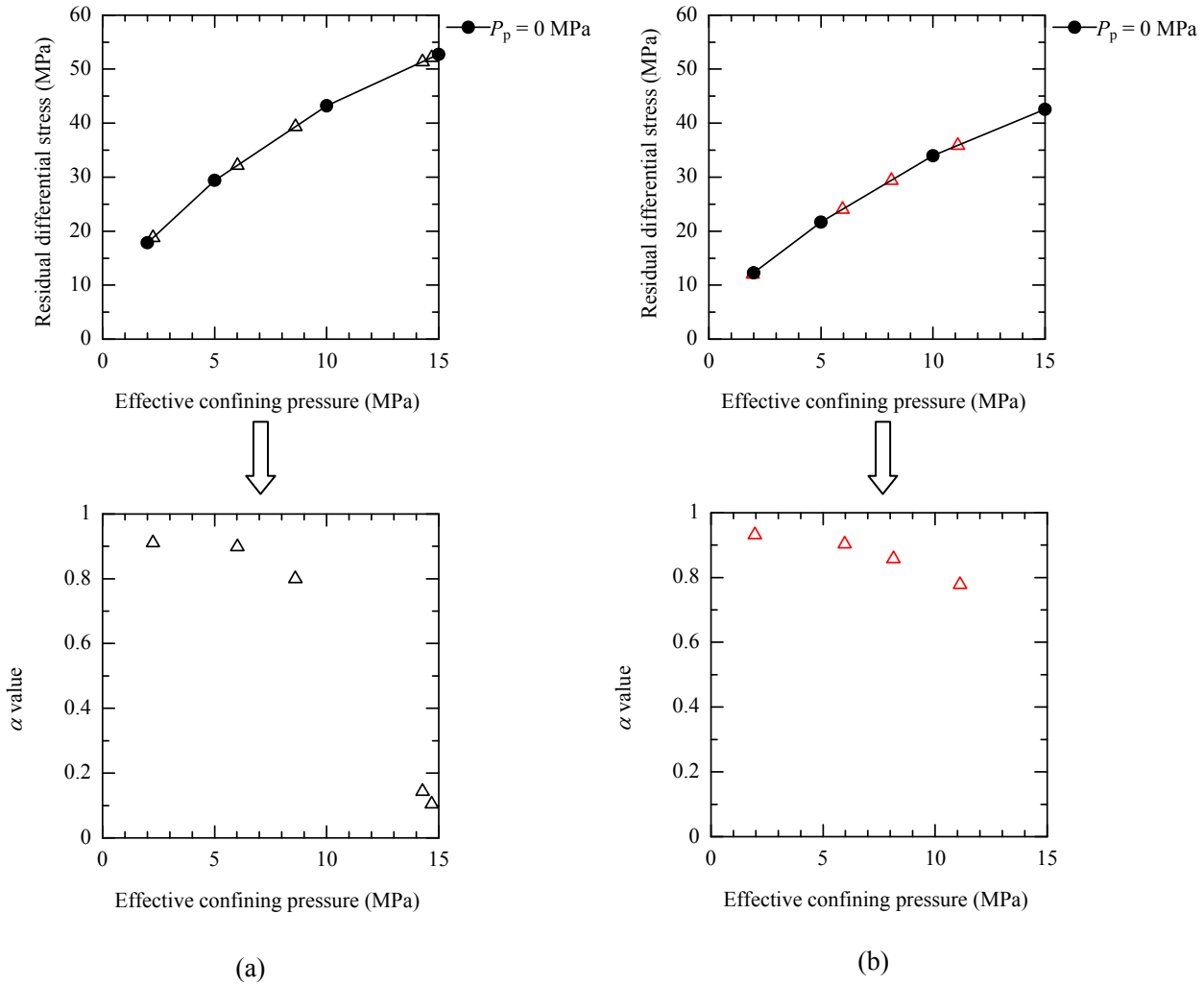


Fig.2.19 Residual differential stresses in multi stage MFEM- a) Multistage MFEM-Descending Pc b) Multistage MFEM-Ascending Pc.

*2.2.3.2 Effective stress coefficients by Hydrostatic compression test*

In the drained hydrostatic compression test with zero pore pressure, the bulk modulus of the intact rock, $K$ increased with the hydrostatic pressure, as shown in Fig. 2.11. This was attributed to the closure of microcracks and elliptical pores. As a consequence, $\alpha_{\text{-Biot's}}$ decreased with increasing confining pressure, and was in the range $1 > \alpha_{\text{-Biot's}} > 0.8$, as shown in Fig. 2.20. The effective stress coefficients by hydrostatic tests for fractured rock, $\alpha_{\text{-Fractured}}$ were larger than those for intact rock $\alpha_{\text{-Biot's}}$ and were close to unity (Fig. 2.20).

*2.2.3.3 General review of Effective stress coefficients for Kimachi sandstone*

The coefficients $\alpha_{\text{-Peak}}$ were significantly lower than those for intact rock under hydrostatic conditions or $\alpha_{\text{-Biot's}}$. For residual strength, the most reliable $\alpha_{\text{-Residual}}$ by multistage MFEM ascending $P_c$ approach was almost the same as $\alpha_{\text{-Biot's}}$ (Fig. 2.20).

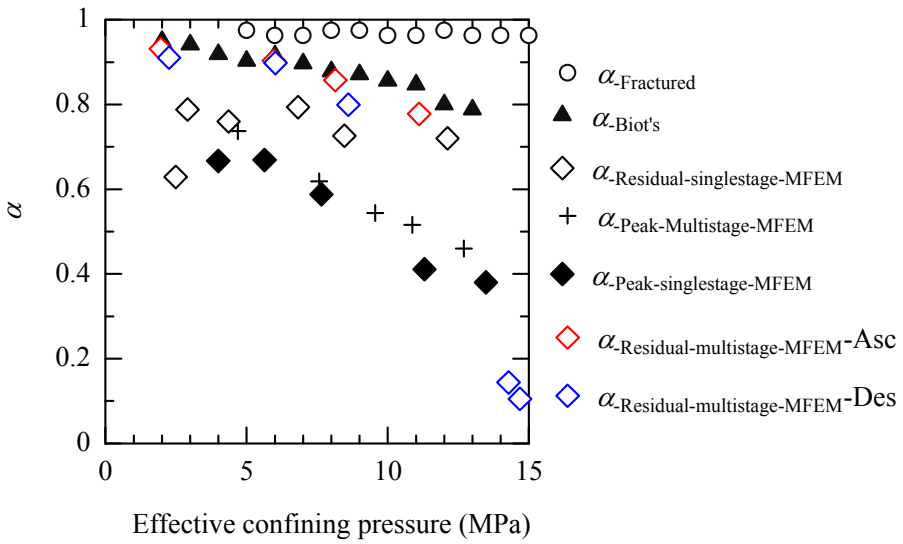


Fig. 2.20 Summary of effective stress coefficients for Kimachi sandstone with effective confining pressure.

Assuming Eq. (2.8) for the effective stress coefficient, the constants $A$ and $B$ can be obtained as illustrated in Fig. 2.21 (Table 2.4). By altering Eq. (2.8), Eq. (2.9) can be obtained. Hence the effective stress coefficient can be calculated by substituting $P_C$, $P_P$, $A$ and $B$. The low coefficient of correlations for $\alpha_{\text{-Fracture}}$ and $\alpha_{\text{-Residual}}$ suggest that they are almost constant.

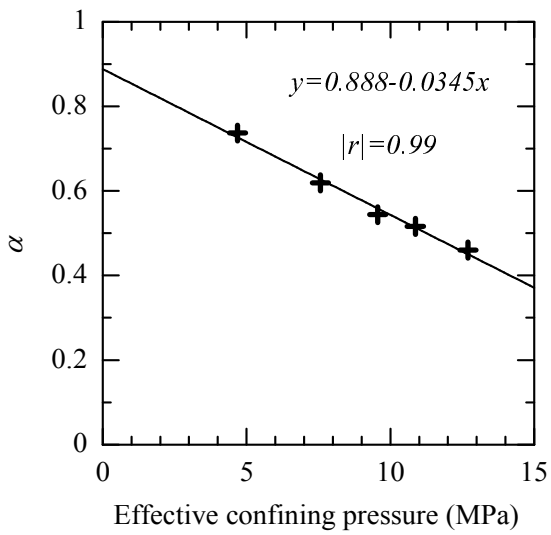


Fig. 2.21 An example of approximation by Eq.2.8 (Multistage MFEM).

$$\alpha = A - BP_{\mathrm{c}}' \tag{2.8}$$

$$\alpha = \frac{A - BP_{\mathrm{c}}}{1 - BP_{\mathrm{p}}} \tag{2.9}$$

Table 2.4. Constant $A$ and $B$ in Eq.2.8 and Eq.2.9

| Effective stress coefficients | $A$ | $B$ (MPa$^{-1}$) | Coefficient of correlation $\lvert r \rvert$ |
|---|---|---|---|
| $\alpha$-$_{\text{Biot's}}$ | 0.984 | 0.014 | 0.97 |
| $\alpha$-$_{\text{Fractured}}$ | 0.974 | 0.001 | 0.36 |
| $\alpha$-$_{\text{Peak}}$ (single stage MFEM) | 0.834 | 0.035 | 0.98 |
| $\alpha$-$_{\text{Peak}}$ (multistage MFEM) | 0.888 | 0.034 | 0.99 |
| $\alpha$-$_{\text{Residual}}$ (single stage MFEM) | 0.727 | -0.001 | 0.09 |

## 2.3. Discussion

### *2.3.1 Applicability of the MFEM*

MFEMs were successfully applied for the determination of effective stress coefficients for the peak and residual strengths ($\alpha_{\text{-Peak}}$ and $\alpha_{\text{-Residual}}$) and multistage MFEM is recommended to obtain the effective stress coefficients for peak strength and multistage MFEM- ascending $P_c$ approach is recommended to obtain effective stress coefficients for residual strength. The strength correction in the multistage MFEM is particularly effective in obtaining results with a small amount of data scattering.

Reproducibility of the MFEM was not directly investigated in present work. Though, the coincident between $\alpha_{\text{-Peak}}$ by single stage and multistage tests indirectly suggests that reproducibility was fairly high.

### *2.3.2 Relationship between the coefficient for intact rock and strengths*

The effective stress coefficients for peak strength, residual strength and for the intact rock ($\alpha_{\text{-Peak}}$, $\alpha_{\text{-Residual}}$ and $\alpha_{\text{-Biot's}}$), can be well described using a linear fit, taking the effective normal stress ($\sigma_n'$) on the rupture plane as the $x$-axis, as shown in Fig. 2.22 (assuming that the rupture plane is inclined by 30º). Assuming Eq. (2.10) for the effective stress coefficient, the constants $A$ and $B$ can be obtained.

$$\alpha = A - B\sigma_n' \tag{2.10}$$

This means that, $\alpha$ for intact rock, peak and the residual strengths can be evaluated based on normal stress as,

$$\alpha = \frac{A - B\sigma_n}{1 - BP_p} \tag{2.11}$$

Where A = 0.976 and B =0.0096 ($MPa^{-1}$) for this rock.

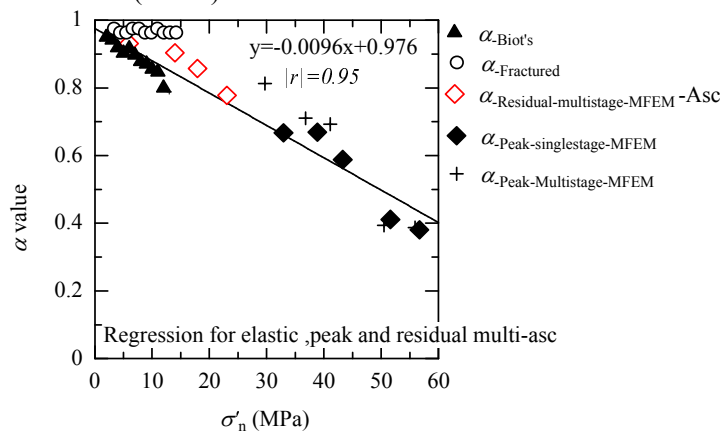


Fig. 2.22 Effective normal stress vs $\alpha$ relationship for Kimachi sandstone.

# 3. Experiment on
# Bibai sandstone

### 3.1 Materials and Method

Bibai sandstone was sampled just above a coal seam at an open pit in Sambi Coal Mine in Bibai, Hokkaido, Japan. Bibai sandstone was classified into arenite sandstone with little matrix. It was mainly formed of coarse sand particles consists of quartz particles (< 1 mm) from granite, slate fragments, mudstone fragments, and siliceous mudstone and chert fragments (< 1.4 mm) which include a few illite and chlorite. Matrix is less than 1% and mainly consists of illite. The rock also has thin seams of coal. No expansive clay mineral could be found. The physical properties of the rock are shown in Table 3.1.

Table 3.1: Physical properties of the Bibai sandstone shown as "average value (number of specimen) ± standard deviation". UCS: Uniaxial Compressive Strength.

| $V_p$ of specimen (km/s) | $V_s$ of specimen (km/s) | Dry density (g/cm$^3$) | Effective porosity (%) | UCS (saturated) (MPa) |
|---|---|---|---|---|
| 2.941 (3) ± 0.028 | 1.245(3) ± 0.026 | 2467 (10)± 12 | 5.79 (10) ± 0.22 | 101.9 (2) ± 2.3 |

Experimental method (specimen and sample preparation; experimental setup; experimental procedure; and micro- and macrostructure analysis) was the same as section 2.1.

### 3.2 Results

*3.2.1. Deformation of rocks*

It was confirmed that either peak or residual strength increased with increasing confining pressure and decreased with increasing pore pressure (Fig. 3.2). There is no obvious difference between the strengths obtained by single (Fig. 3.2a) and multistage (Fig. 3.2c) triaxial test.

An increase in the peak and residual strengths was clearly observed as the confining pressure increased, and brittle failure was exhibited for all confining pressures, as shown in Fig.3.1a. The opposite occurred when the pore pressure was introduced, as shown in Fig.3.1b, the peak and residual strengths decreased with increasing pore pressure.

With small confining pressures of 2 MPa and 5 MPa, the rock exhibited a nonlinear stress–strain relation (see Fig. 2.2a), which typically is attributed to the closure of pre-existing elliptical pores and microcracks. However, at higher confining pressures of 10 MPa and 15 MPa, the phase corresponding to closure at the initial stage of the stress–strain curve was not distinct, which suggests that microcrack closure already occurred before axial loading under the high confining pressures. Following the closure phase, all the specimens deformed elastically.

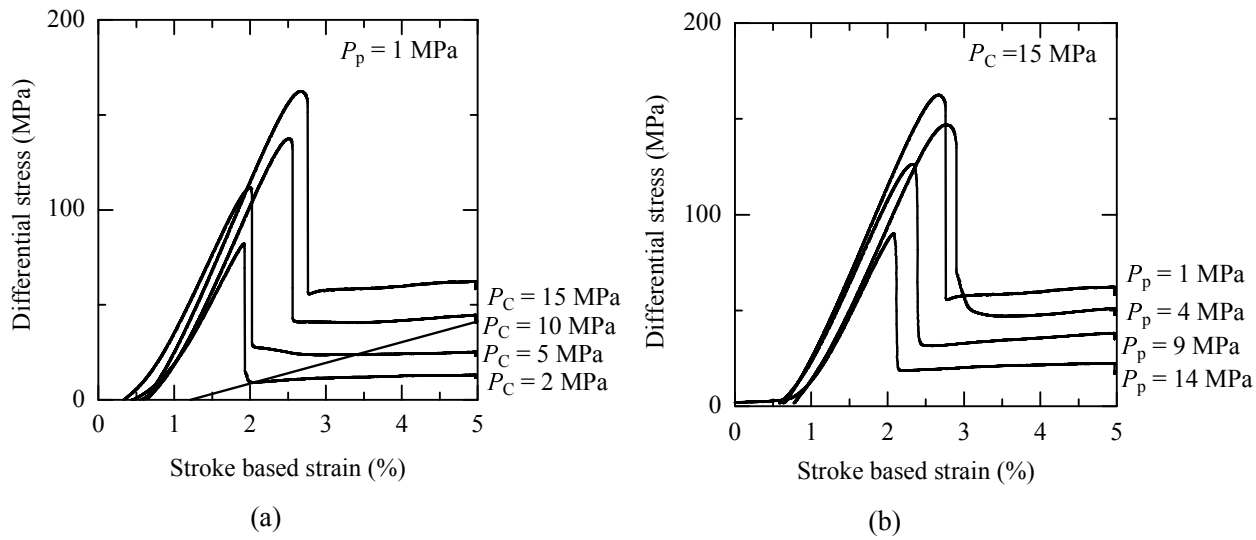


Fig. 3.1 Differential stress versus stoke based strain for different confining pressures and pore pressures. a) Effect of confining pressure b) Effect of pore pressure.

As in Kimachi sandstone, difference cannot be observed in the amount of the magnitude of permanent set with increasing confining pressure.

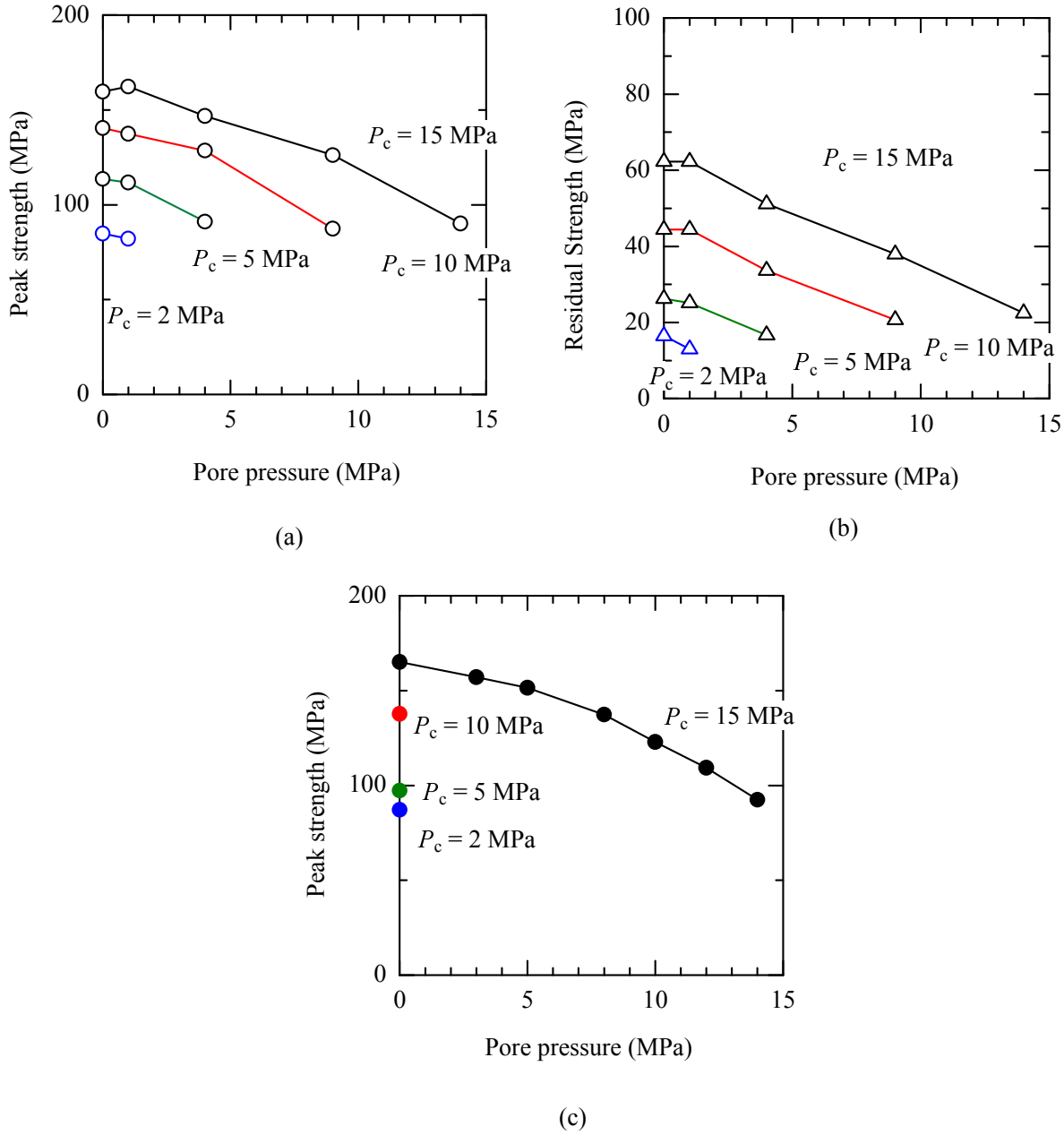


Fig. 3.2 (a) Peak strength with pore pressure for different confining pressures (b) Residual strength with pore pressure for different confining pressures for single stage triaxial tests. (c) Peak strength with pore pressure for multistage triaxial test.

Residual differential stresses obtained by descending $P_c$ approach (Figs .3.3 and 3.4) of multistage triaxial tests is less than ascending $P_c$ approach by approximately 20% (Figs .3.5 and 3.6) except $P$c = 15

MPa $P_p$ = 14 MPa step which was the last step of descending $P_c$ method with non zero pore pressure and first step of ascending $P_c$ method with non zero pore pressure. This would be a result of heterogeneity of the specimens and suggests that the compaction did not occur under high effective confining pressure.

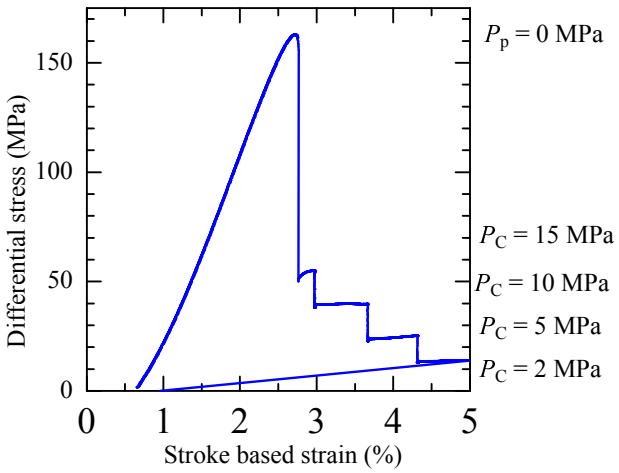


Fig. 3.3 Differential stress versus stoke based strain graph for the sample tested *Multistage triaxial tests* -Descending $P_c$ method with zero pore pressure

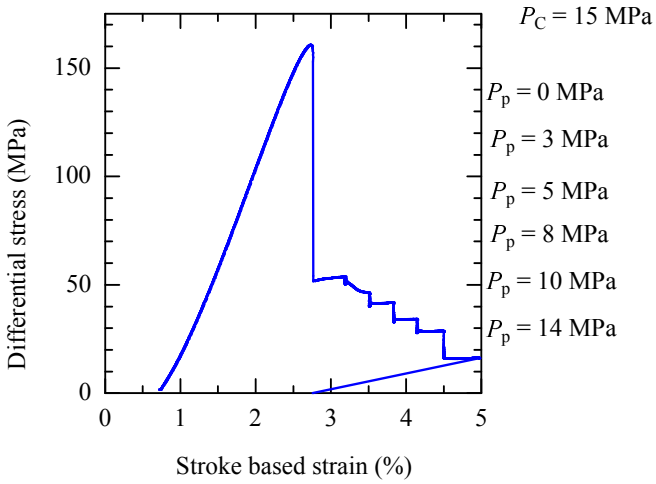


Fig. 3.4 Differential stress versus stoke based strain graph for the sample tested *Multistage triaxial tests* -Descending $P_c$ method with non zero pore pressure

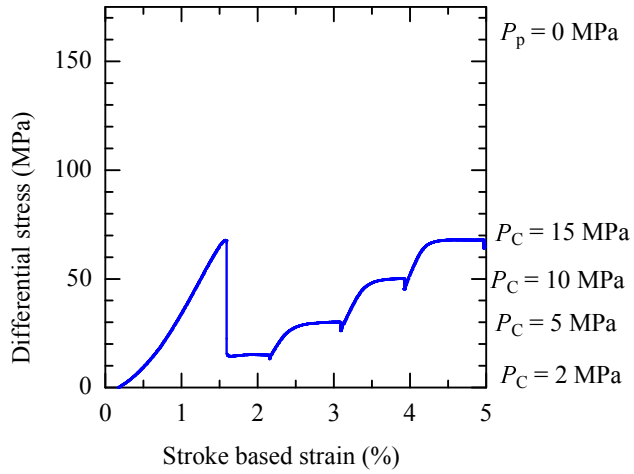


Fig. 3.5 Differential stress versus stoke based strain graph for the sample tested *Multistage triaxial tests* -Ascending $P_c$ method with zero pore pressure

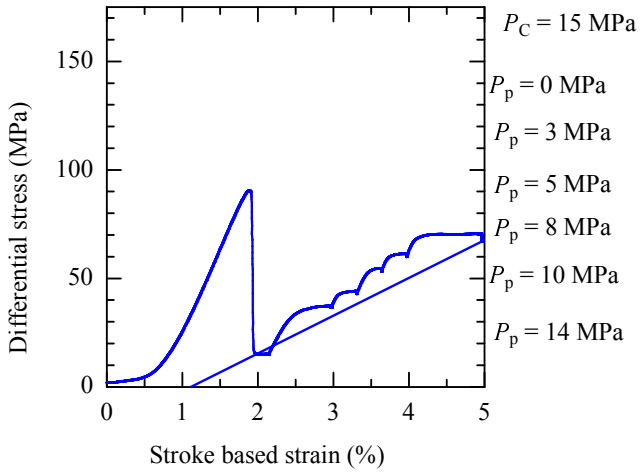


Fig. 3.6 Differential stress versus stoke based strain graph for the sample tested *Multistage triaxial tests* -Ascending $P_c$ method with non zero pore pressure

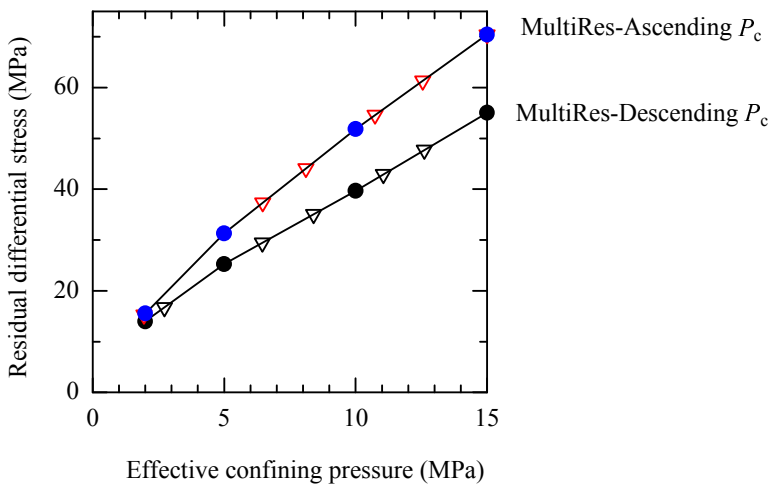


Fig. 3.7 Residual differential stresses in multi stage MFEM

*3.2.2 Micro- and macrostructures*

From the blue resin-impregnated thin-section analysis, the thickness of the rupture plane of Bibai sandstone specimen after axial compression at 2 MPa was much wider than the thickness of the rupture at 15 MPa (Fig. 3.8).

From CT observations, only one rupture plane was observed after axial compression of Bibai sandstone with 15 MPa confining pressure with 1 MPa pore pressure and 15 MPa confining pressure with 4 MPa pore pressure, whereas one main rupture plane and one sub-rupture plane appeared under 15 MPa confining pressure and 9 MPa pore pressure. Main and sub-rupture planes occurred as well as several fractures in the CT image for 15 MPa confining pressure and 14 MPa pore pressure.

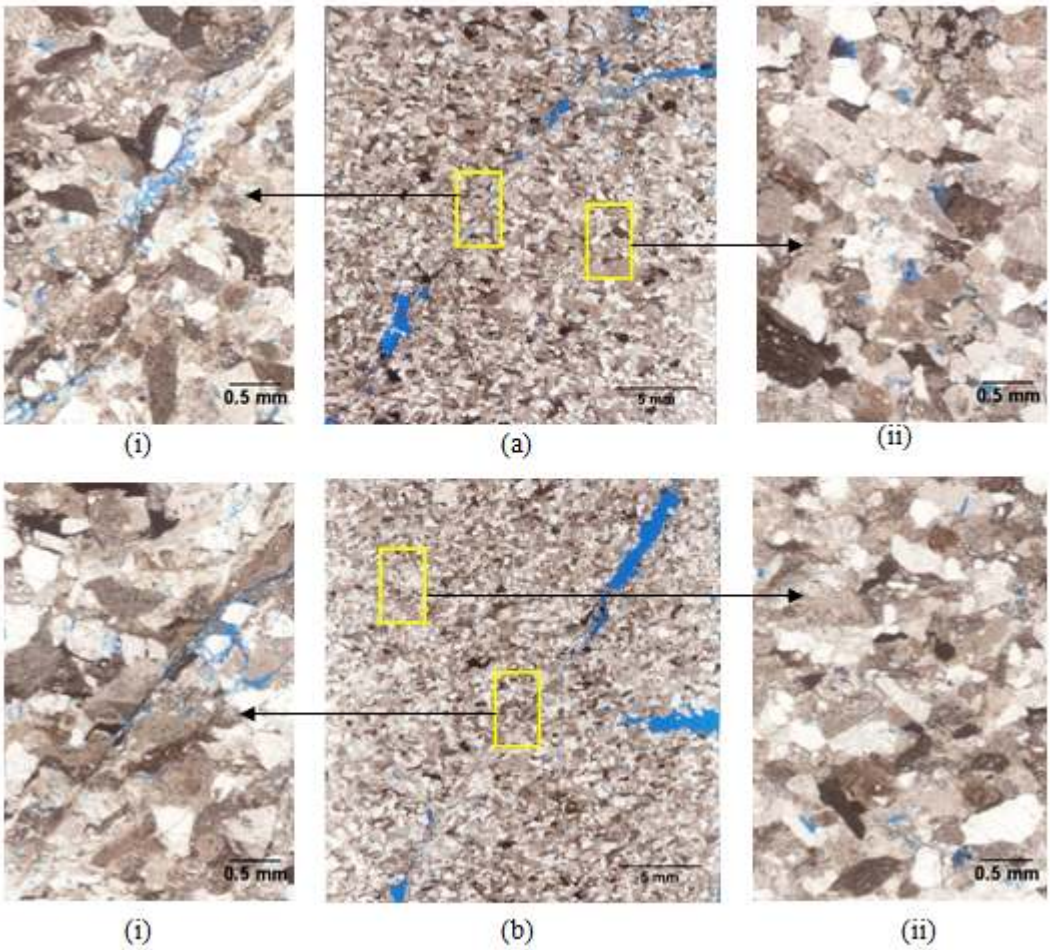


Fig. 3.8 Specimen, blue resin-impregnated thin-section images of post-compression Bibai sandstone specimens at (a) 2 MPa (i) near the shear plane and (ii) far from the shear plane (b) 15 MPa (i) near the shear plane and (ii) far from the shear plane

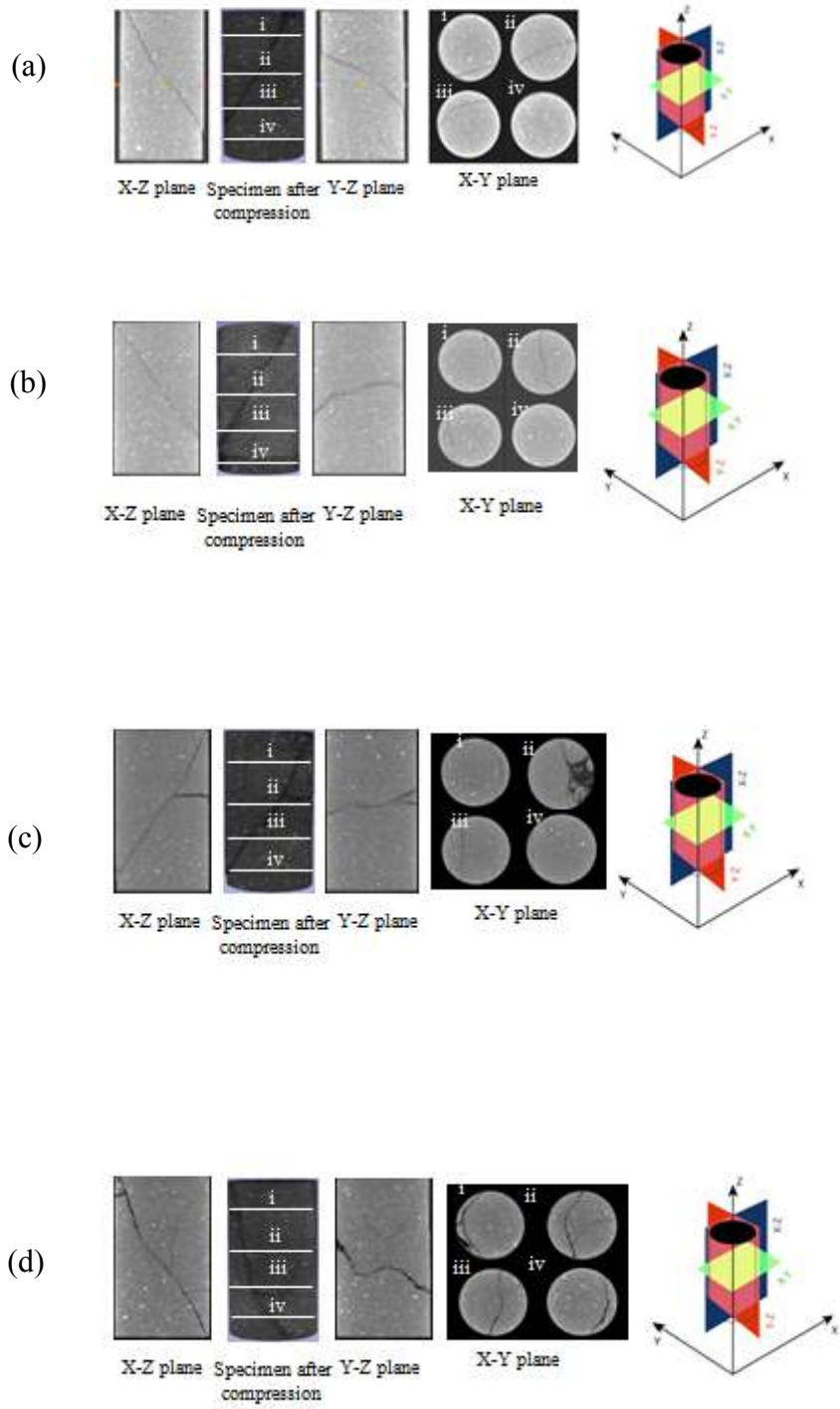


Fig. 3.9 Specimen, CT images after axial compression of Bibai sandstone with 15 MPa confining pressure and (a) 1MPa pore pressure (b) 4 MPa pore pressure (c) 9 MPa pore pressure and (d) 14 MPa pore pressure

*3.2.3 Effective stress coefficients*

*3.2.3.1 Effective stress coefficients by MFEM*

Effective stress coefficients for peak and residual strengths were obtained from maximum differential stress and differential stress in the residual strength state, respectively (Fig. 3.10). In this analysis, stress data related to 1 MPa pore pressure were omitted as the small $P_p$ magnitude caused large errors in $\alpha$ value. The effective stress coefficients for the peak strength, $\alpha$-$_{Peak}$ decreased with increasing effective confining pressure and was in the range $0.9 > \alpha_{\text{-Peak}} > 0.4$, under both single and multi stage MFEMs, as shown in Fig. 3.12. The increased axial stress with confining pressure would have increased the grain to grain contact area and hence effective stress coefficient increased with increasing effective confining pressure.

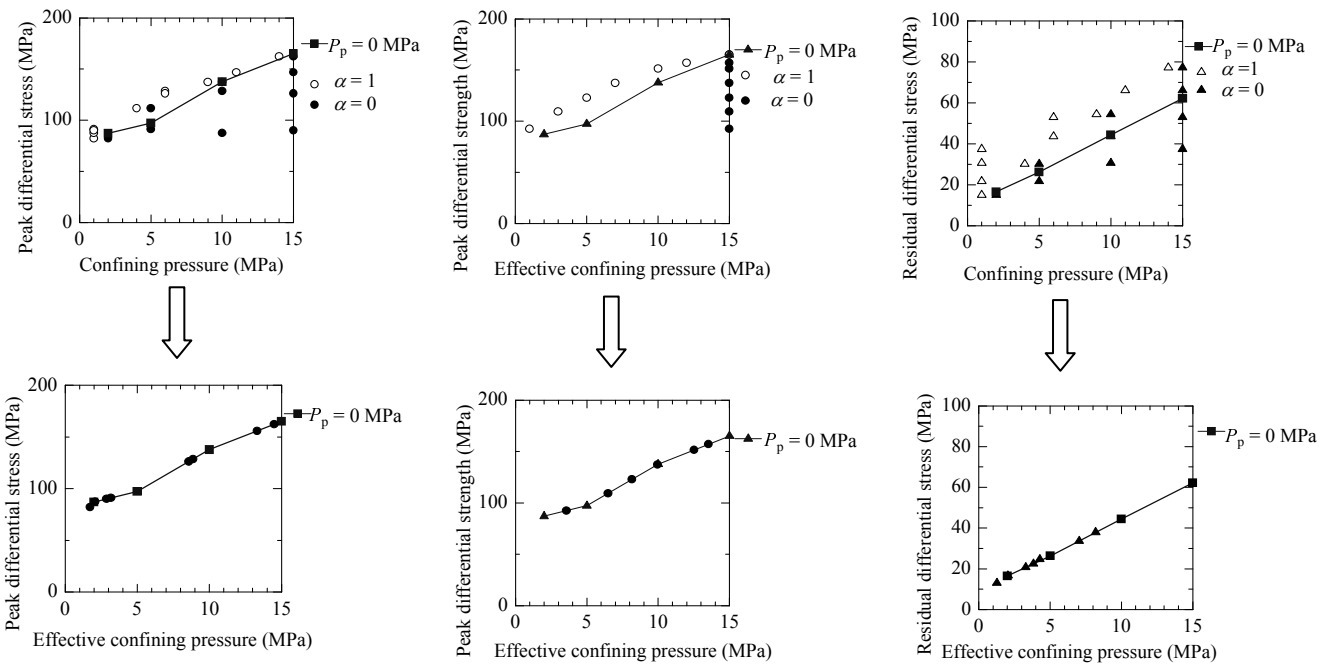


Fig. 3.10 Peak differential stresses in (a) single stage MFEM (b) Multistage MFEM and (c) Residual differential stresses in single stage MFEM

For residual strength, $\alpha$-$_{Residual}$ was almost constant under single stage MFEM and slightly fluctuate in the range of $0.8 > \alpha_{Residual} > 0.7$ (Fig. 3.12). But it shows decrease with increasing effective confining pressure in both approaches of multistage MFEM (Fig 3.12).

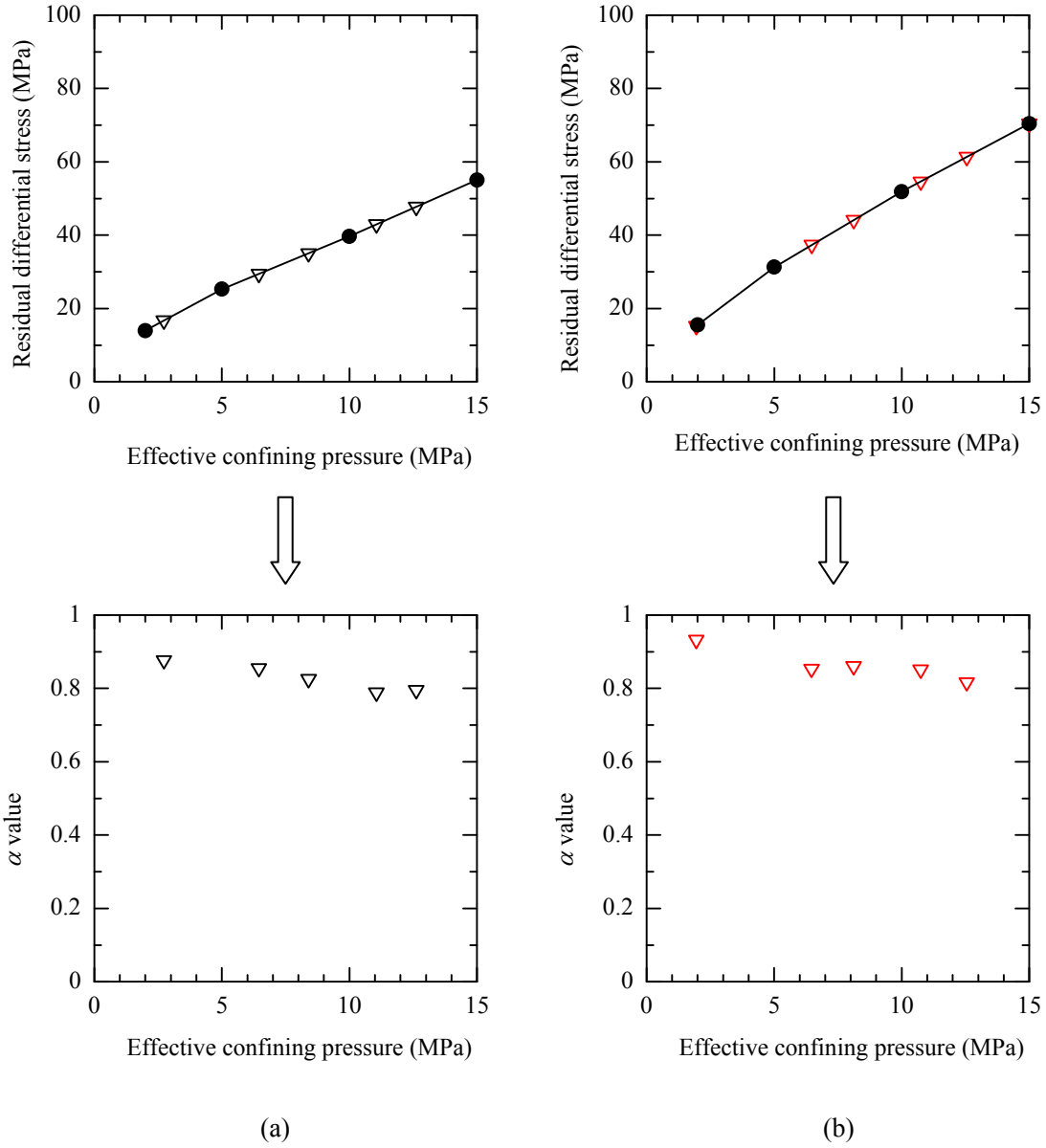


Fig. 3.11 Residual differential stresses in multi stage MFEM (a) Multistage MFEM-Descending *P*c (b) Multistage MFEM-Ascending *P*c.

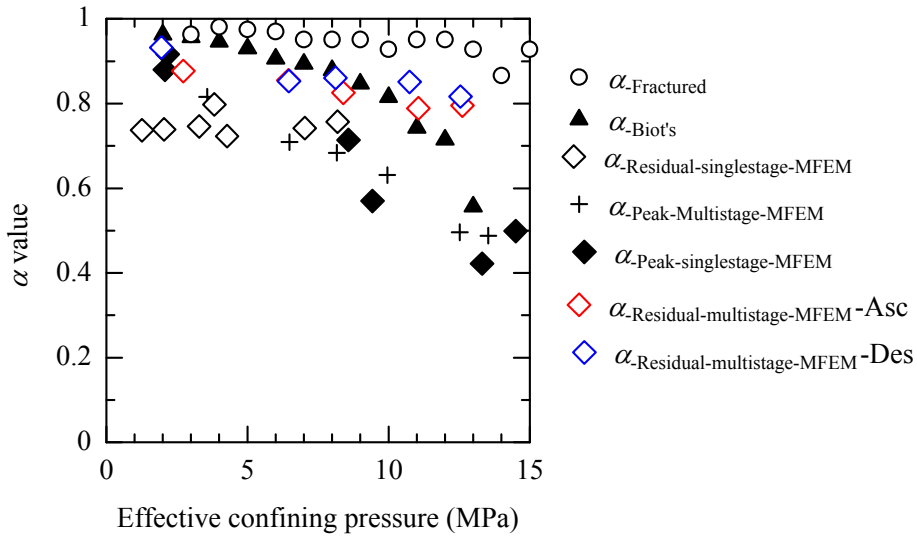


Fig. 3.12 Summary of effective stress coefficients

*3.2.3.2 Effective stress coefficients by Hydrostatic compression test*

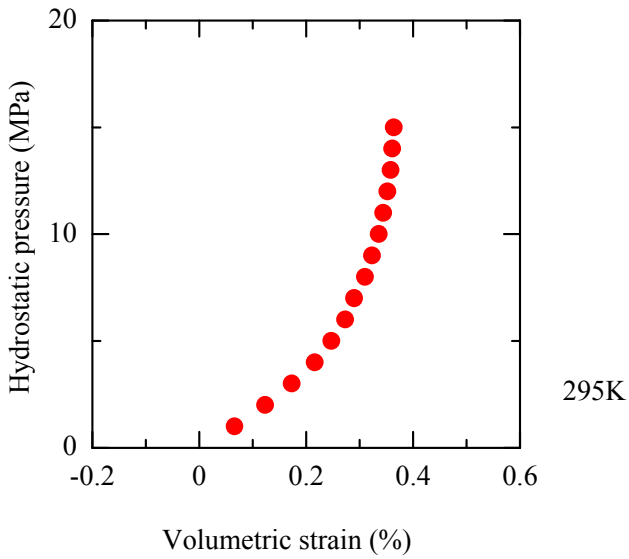


Fig. 3.13 Stress-strain curve in hydrostatic compression test for $P_p = 0$

In the drained hydrostatic compression test with zero pore pressure, the bulk modulus of the intact rock increased with the hydrostatic pressure, as shown in Fig. 3.13. This was attributed to the closure of microcracks and elliptical pores. As a consequence, $\alpha_{\text{-Biot's}}$ decreased with increasing confining pressure, and was in the range $1 > \alpha_{\text{-Biot's}} > 0.5$, as shown in Fig. 3.12. In the drained hydrostatic compression test with non zero pore pressure, the initial part of the curve is not linear (Fig. 3.14) as in the case of Kimachi sandstone. This could be due to lack of contact between the strain gages and the specimen under small hydrostatic pressure.

The effective stress coefficients by hydrostatic tests for fractured rock, $\alpha_{\text{-Fractured}}$ were larger than those for intact rock $\alpha_{\text{-Biot's}}$ and were close to unity (Fig. 3.12).

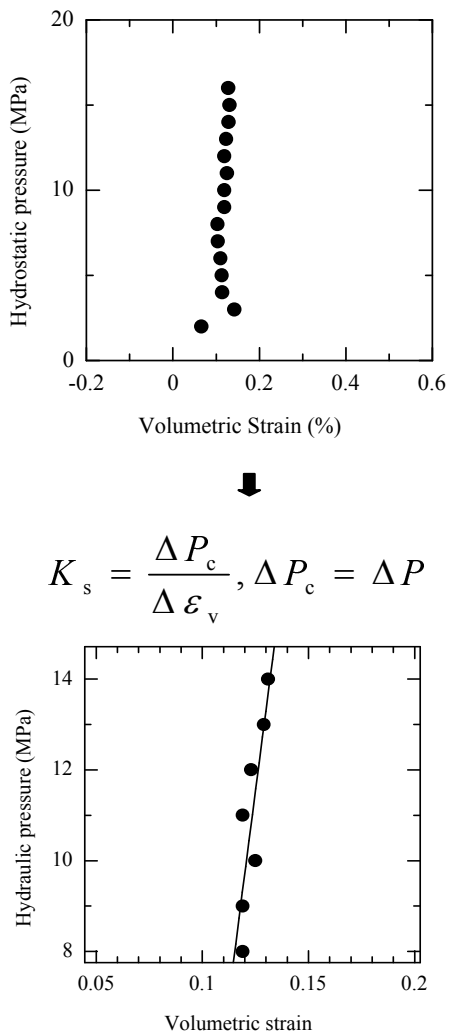


Fig. 3.14 Stress-strain curve in hydrostatic compression test with non zero pore pressure: $\Delta P_c = \Delta P_p$.

*3.2.3.3 General review of Effective stress coefficients for Bibai sandstone*

The coefficients $\alpha_{\text{-Peak}}$, were significantly lower than those for intact rock under hydrostatic conditions or $\alpha_{\text{-Biot's}}$. For residual strength, the most reliable $\alpha_{\text{-Residual}}$ by multistage MFEM ascending $P_c$ approach was almost same as $\alpha_{\text{-Biot's}}$ (Fig. 3.12).

Constant $A$ and $B$ for Eq.2.8 are shown in table 3.2.

Table 3.2 Constant $A$ and $B$ in Eq. 2.8 and Eq. 2.9

| Effective stress coefficients | $A$ | $B$ (MPa$^{-1}$) | Coefficient of correlation $\lvert r \rvert$ |
|---|---|---|---|
| $\alpha_{\text{-Biot's}}$ | 1.040 | 0.024 | 0.958 |
| $\alpha_{\text{-Fractured}}$ | 0.998 | 0.006 | 0.760* |
| $\alpha_{\text{-Peak}}$ (singlestage MFEM) | 0.975 | 0.037 | 0.964 |
| $\alpha_{\text{-Peak}}$ (Multistage MFEM) | 0.942 | 0.034 | 0.989 |
| $\alpha_{\text{-Residual}}$ (singlestage MFEM) | 0.743 | -0.001 | 0.140** |

* $\alpha_{\text{-Fractured}}$ is almost constant.

** Low $|r|$ due to scattering of data.

## 3.3. Discussion

*3.3.1 Applicability of the MFEM*

As in the Kimachi sandstone, MFEMs were successfully applied for the determination of effective stress coefficients for the peak and residual strengths ($\alpha_{\text{-Peak}}$ and $\alpha_{\text{-Residual}}$) of Bibai sandstone. Multistage MFEM is recommended to obtain the effective stress coefficients for peak strength and multistage MFEM-ascending $P_c$ approach is recommended to obtain effective stress coefficients for residual strength. The strength correction in the multistage MFEM is particularly effective in obtaining results with a small amount of data scattering.

The coincident between $\alpha_{\text{-Peak}}$ by single stage and multistage tests indirectly suggests that reproducibility was fairly high.

*3.3.2 Relationship between the coefficient for intact rock and strengths*

As shown in Fig. 3.16, the effective stress coefficient for fractured rock, peak and residual (multi-Asc) strengths could be approximated by eq. (2.10) in which A = 0.95 and B=0.0031 ($MPa^{-1}$).

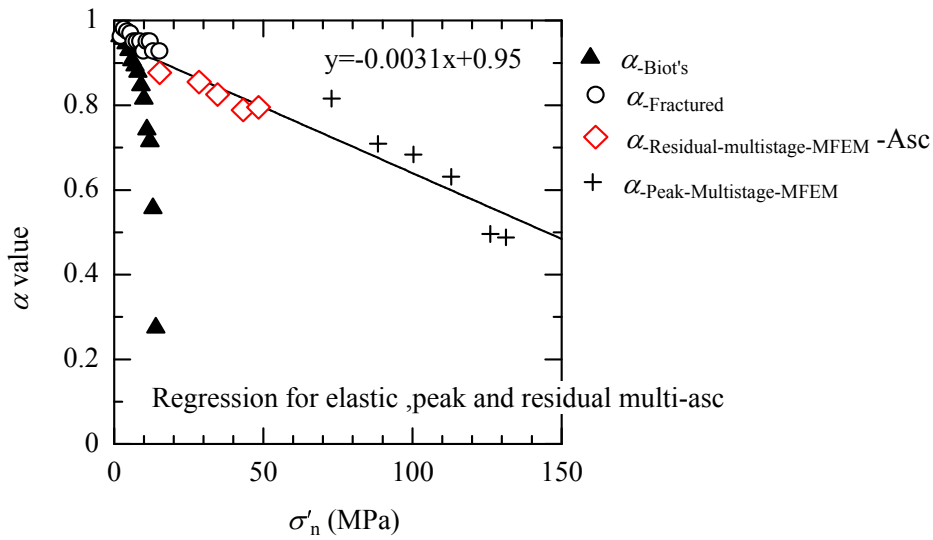


Fig. 3.16 Effective normal stress vs $\alpha$ relationship for Bibai sandstone.

# 4. Experiment on
# Inada granite

### 4.1 Materials and Method

The Inada granite was sampled in Ibaraki, Japan. The composition of the rock was mainly quartz, feldspar, biotite, and allanite, with zircon, apatite, and ilmenite as accessory minerals. The grain sizes of the minerals are 3.0–4.0 mm (on average) for quartz, approximately 2.0–3.0 mm for plagioclase, approximately 2.0–4.0 mm for alkali feldspar, and generally less than 1.0 mm for biotite [Lin & Takahashi 2008]. The physical properties of the rock are listed in Table 4.1.

Table 4.1: Physical properties of the Inada granite shown as "average value (number of specimen) ± standard deviation". UCS: Uniaxial Compressive Strength. [Alam et al., 2014(d)]

| $V_p$ of specimen (km/s) | $V_s$ of specimen (km/s) | Dry density (g/cm$^3$) | Effective porosity (%) | UCS (saturated) (MPa) |
|---|---|---|---|---|
| 2.87 (17) ± 0.07 | 2.09 (17) ± 0.06 | 2.70 (17) ± 0.01 | 0.584 (17) ± 0.023 | 180.9 (2) ±16.9 |

Experimental method (specimen and sample preparation; experimental setup; experimental procedure; and micro- and macrostructure analysis) was the same as section 2.1.

## 4.2 Results

### *4.2.1 Deformation of rocks*

An increase in the peak and residual strengths was clearly observed as the confining pressure increased, and brittle failure was exhibited for all confining pressures, as shown in Fig. 4.1a. The opposite occurred when the pore pressure was introduced, as shown in Fig. 4.1b: the peak and residual strengths decreased with increasing pore pressure.

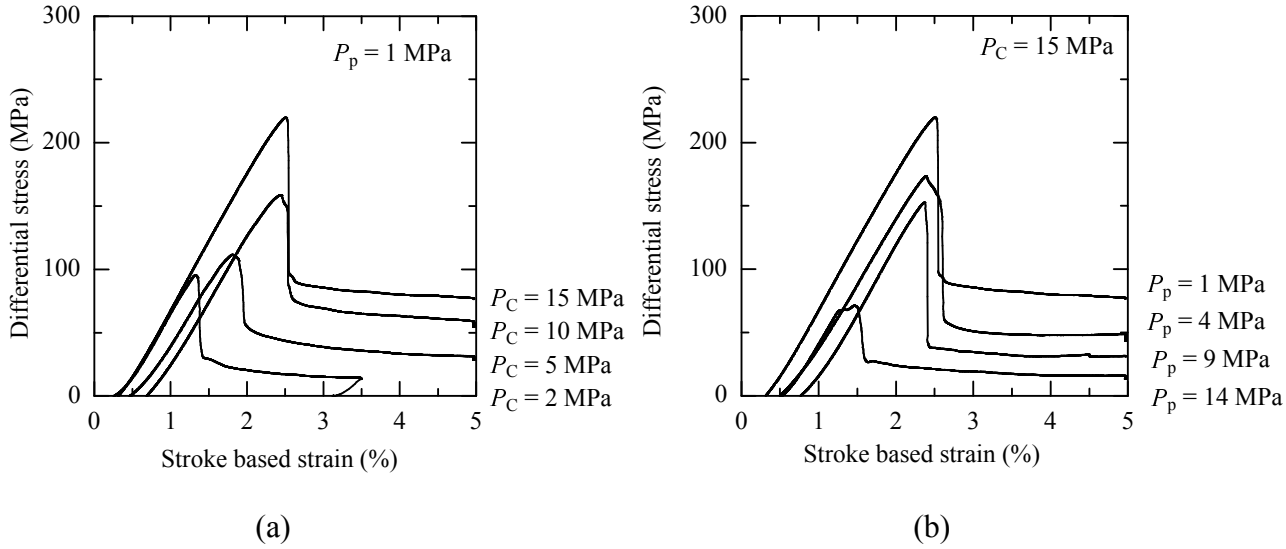


Fig. 4.1 Differential stress versus stoke based strain for different confining pressures and pore pressures. (a) Effect of confining pressure (b) Effect of pore pressure.

### *4.2.2 Micro- and macrostructures*

From the CT analysis conducted by Alam et al (2014) observed a main rupture plane in the X−Z plane, with subrupture planes in the Y−Z plane, at $P_c$ = 1 MPa (Fig. 4.2a). The main rupture plane consisted of a network of microcracks (Fig. 4.2d). Numerous axial cracks from biotite grains were also observed. As described in detail by Nishiyama et al. [Nishiyama et al., 2002], this type of microcracking was induced because biotite is softer than quartz or plagioclase. The distinct single rupture plane in the CT image (Fig. 4.2b) was also observed in the thin section at $P_c$ = 9 MPa (Fig. 4.2e). This rupture plane also consisted of a network of microcracks; however, it had a smaller width than that at $P_c$ = 1 MPa, and axial cracks from biotite were not observed. Multiple rupture planes were observed at $P_c$ = 15 MPa (Fig. 4.2c).

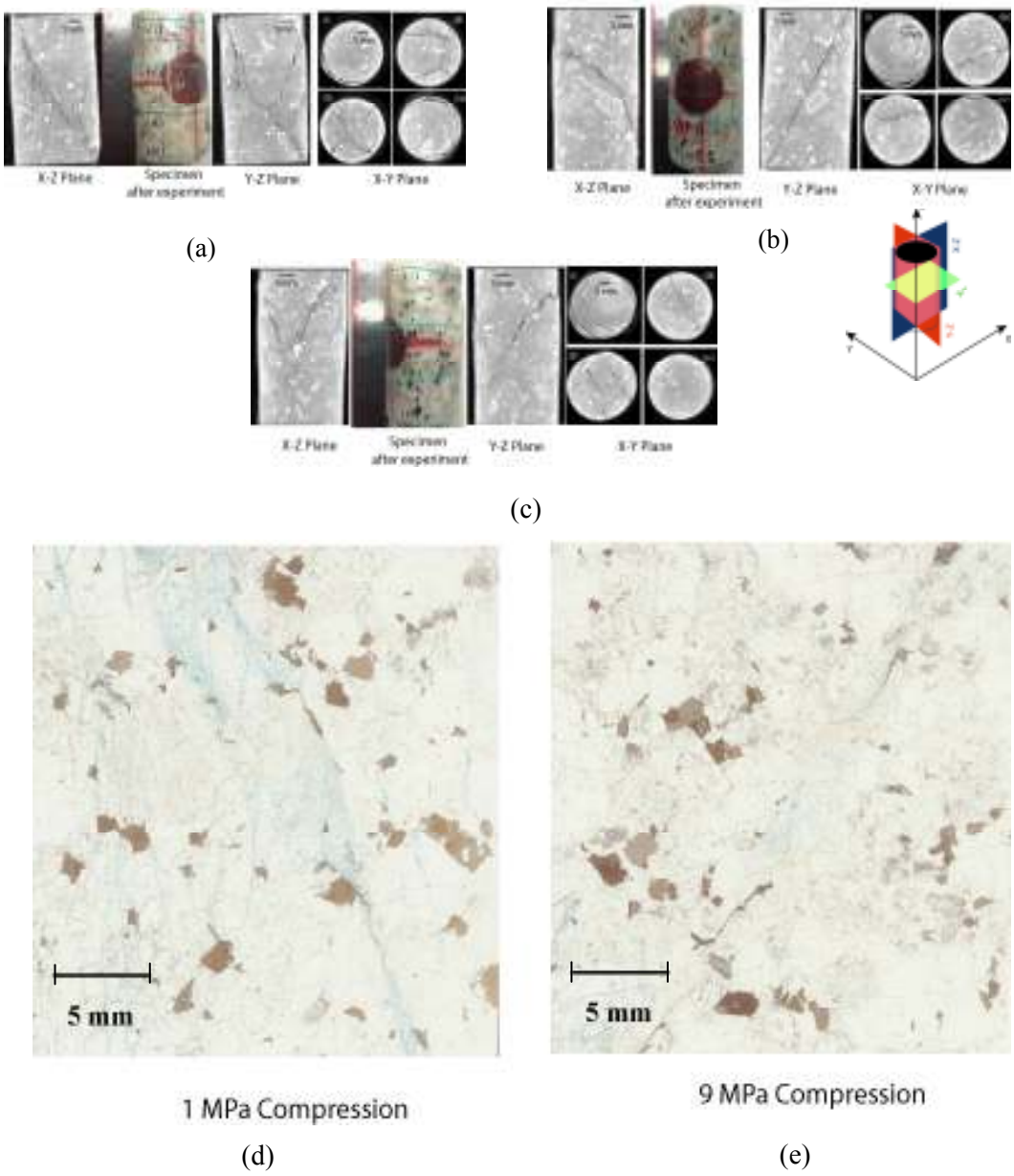


Fig. 4.2 Specimen, CT images, and blue resin-impregnated thin-section images of the specimens after axial compression of Inada granite. Specimen and CT images at (a) 1 MPa, (b) 7 MPa, and (c) 15 MPa. Blue resin-impregnated thin-section image at (d) 1 MPa and (e) 9 MPa. The loading direction is vertical. [Alam et al., 2014, 2013]

*4.2.3 Effective stress coefficients*

*4.2.3.1 Effective stress coefficients by MFEM*

Effective strength coefficients for peak and residual strengths were obtained from maximum differential stress and differential stress in the residual strength state, respectively (Fig. 3.10).

$\alpha$ value for peak strength under the single-stage MFEM were scattered around 1, as shown in Fig. 4.4. At higher effective confining pressures; 10 and 15 MPa, $\alpha$ exhibited more variation, and deviated significantly from 1, as shown in Fig. 4.4. In the multistage triaxial tests, the test steps were terminated immediately before yield due to the brittleness of the rock. The results showed that effective stress coefficient for peak strength decreased with effective confining pressure and were in the range $0.8 > \alpha_{peak} > 0.2$ (see Fig. 4.4). The behavior of $\alpha$ for residual strength by single stage test was significantly scattered. Multistage test was not carried out for residual strength because of the time limitation.

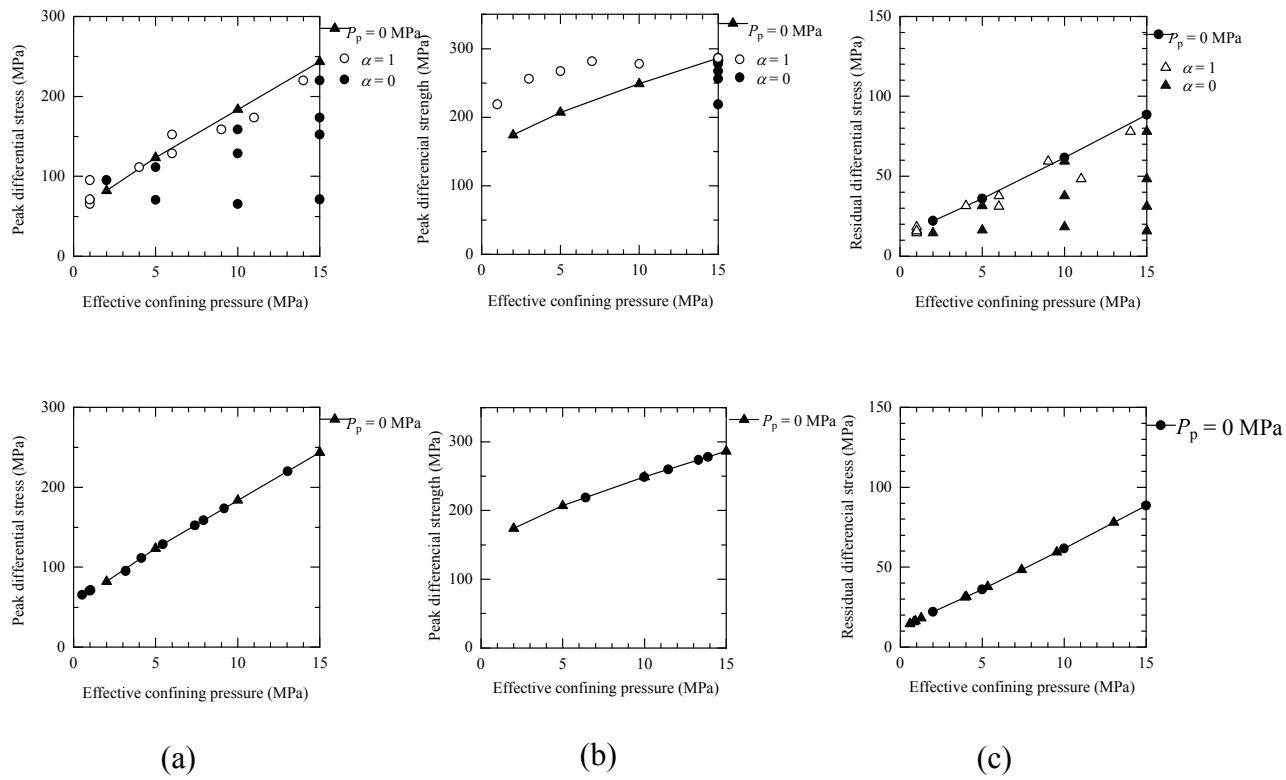


Fig. 4.3 (a) Peak differential stresses in single stage MFEM (b) Peak differential stresses in multistage MFEM and (c) Residual differential stresses in single stage MFEM

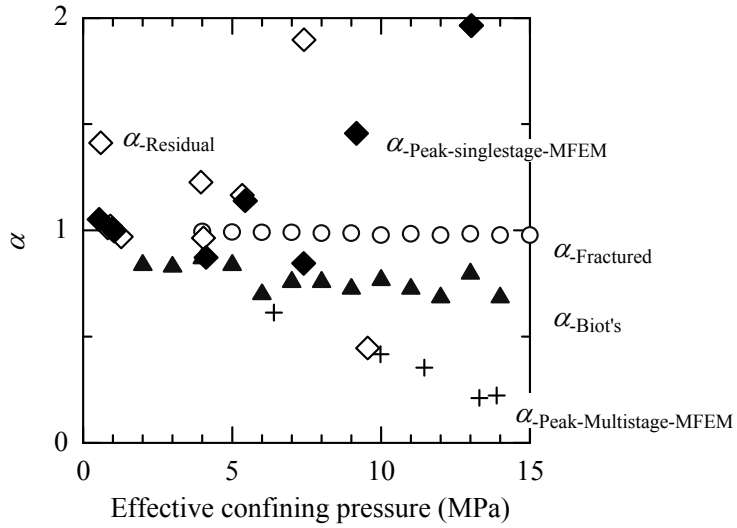


Fig. 4.4 Summary of effective stress coefficients

*4.2.3.2 Effective stress coefficients by Hydrostatic compression test*

In the drained hydrostatic compression tests with zero pore pressure, the bulk modulus of the intact rock increased with the hydrostatic pressure, as shown in Fig. 4.5, which was attributed to the closure of microcracks.

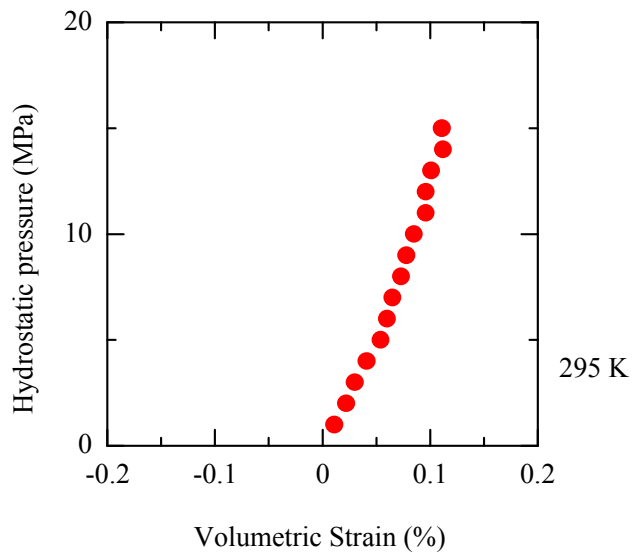


Fig. 4.5 Stress-strain curve in hydrostatic compression test for $P_p$=0

As a consequence, the effective stress coefficient decreased with confining pressure and was in the range $0.9 > \alpha_{\text{-Biot's}} > 0.7$ as shown in Fig. 4.4. These results exhibited rather large variations in $\alpha$, which was attributed to the small strain. The effective stress coefficients by hydrostatic tests for fractured rock, $\alpha_{\text{-Fractured}}$ were larger than those for intact rock $\alpha_{\text{-Biot's}}$ and were close to unity (Fig. 4.4).

In the drained hydrostatic compression test with non zero pore pressure, the initial part of the curve is not linear (Fig. 4.6) as in the case of both type of sandstones. This could be due to lack of contact between the strain gages and the specimen under small hydrostatic pressure.

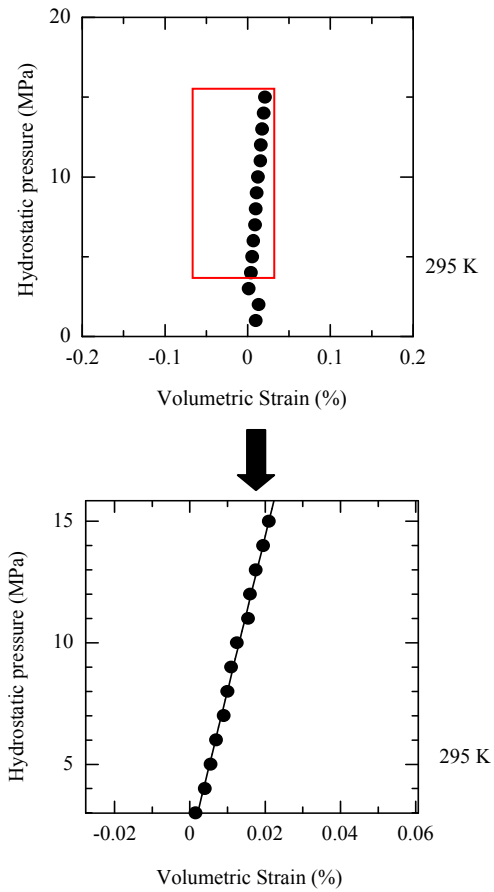


Fig. 4.6 Stress-strain curve in hydrostatic compression test with non zero pore pressure: $\Delta P_c = \Delta P_p$.

*4.2.3.3 General review of Effective stress coefficients for Inada granite*

The coefficients $\alpha_{\text{-Peak}}$, were significantly lower than those for intact rock under hydrostatic conditions or $\alpha_{\text{-Biot's}}$.

Assuming Eq. (2.8) for the effective stress coefficient, the constants *A* and *B* can be obtained.

Constant *A* and *B* for Eq.2.8 are shown in table 4.2.

Table 4.2 Constant *A* and *B* in Eq. 2.8 and Eq. 2.9

| Effective stress coefficients | A | B ($MPa^{-1}$) | coefficient of correlation \|r\| |
|---|---|---|---|
| Intact | 0.858 | 0.0113 | 0.7 |
| Fractured | 1 | 0.0015 | 0.9 |
| Peak(multi) | 0.96 | 0.054 | 0.99 |

**4.3 Discussion**

*4.3.1 Applicability of the MFEM*

Only the multistage MFEM was applicable for Inada granite and it is also to determine the effective stress coefficients for the peak strengths, $\alpha_{\text{-Peak}}$. Applicability of multistage MFEM for $\alpha_{\text{Residual}}$ was not examined because of the time limitation.

*4.3.2 Relationship between the coefficient for intact rock and strengths*

As shown in Fig. 4.7, the effective stress coefficient for Inada granite could not be accurately described using a linear fit. Allowing rather large error, however, a very rough estimation might be possible.

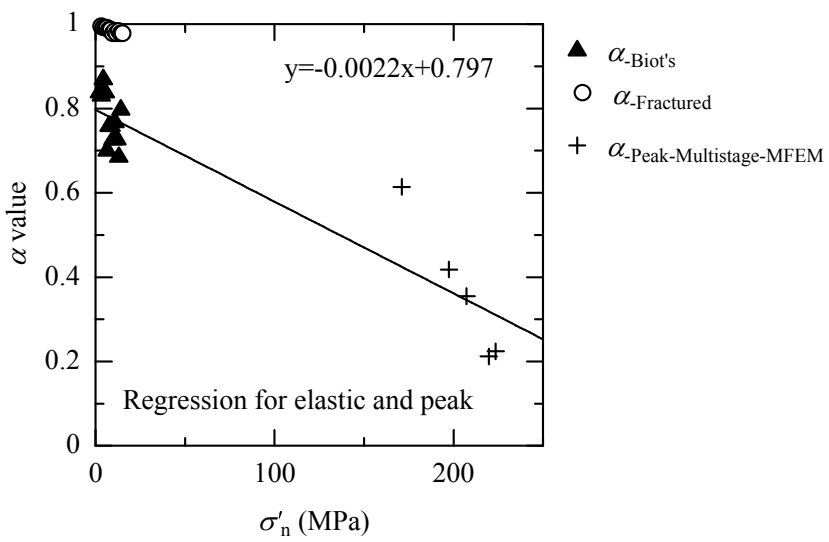


Fig. 4.7 Effective normal stress vs $\alpha$ relationship for Inada granite

# 5. Experiment on

# Shikotsu welded tuff

## 5.1 Materials and Method

### 5.1.1 *Specimen and sample preparation*

The Shikotsu welded tuff was sampled at Hokkaido, Japan, and consists of plagioclase, hypersthene, augite, hornblende, and transparent glass having a felt-like structure with amoebic form in the matrix. The grain sizes of the minerals are 0.3−1.5 mm for plagioclase, about 0.5 mm for hypersthene, 0.3–0.7 mm for augite, and 0.5−1.0 mm for hornblende [Doi, 1963]. The physical properties of the rock are listed in Table 5.1.

Table 5.1: Physical properties of the Shikotsu welded tuff shown as "average value (number of specimen) ± standard deviation". UCS: Uniaxial Compressive Strength [Alam et al., 2014(d)].

| $V_p$ of specimen (km/s) | $V_s$ of specimen (km/s) | Dry density (g/cm$^3$) | Effective porosity (%) | UCS (saturated) (MPa) |
|---|---|---|---|---|
| 1.745 (2) ± 0.007 | 1.245(2) ± 0.021 | 1.304 (10)± 0.012 | 36.5 (10) ± 2.3 | 13.53 (2) ± 2.74 |

Experimental method (specimen and sample preparation; experimental setup; experimental procedure; and micro- and macrostructure analysis) was the same as section 2.1.

## 5.2 Results

### *5.2.1 Deformation of rocks*

With a constant pore pressure of 1 MPa, the Shikotsu welded tuff exhibited strain softening behavior with small confining pressures of 2 MPa and 5 MPa, and almost perfect plastic behavior with a confining pressure of 10 MPa, as shown in Fig. 5.1a. For a confining pressure of 15 MPa, the rock did not exhibit a clear peak strength, and it exhibited strain hardening for strains greater than 1.5%. At $P_c$ > 10 MPa, i.e., strain hardening, the yield stress decreased slightly with increasing confining pressure and the residual strength increased with the confining pressure (Fig. 5.1a).

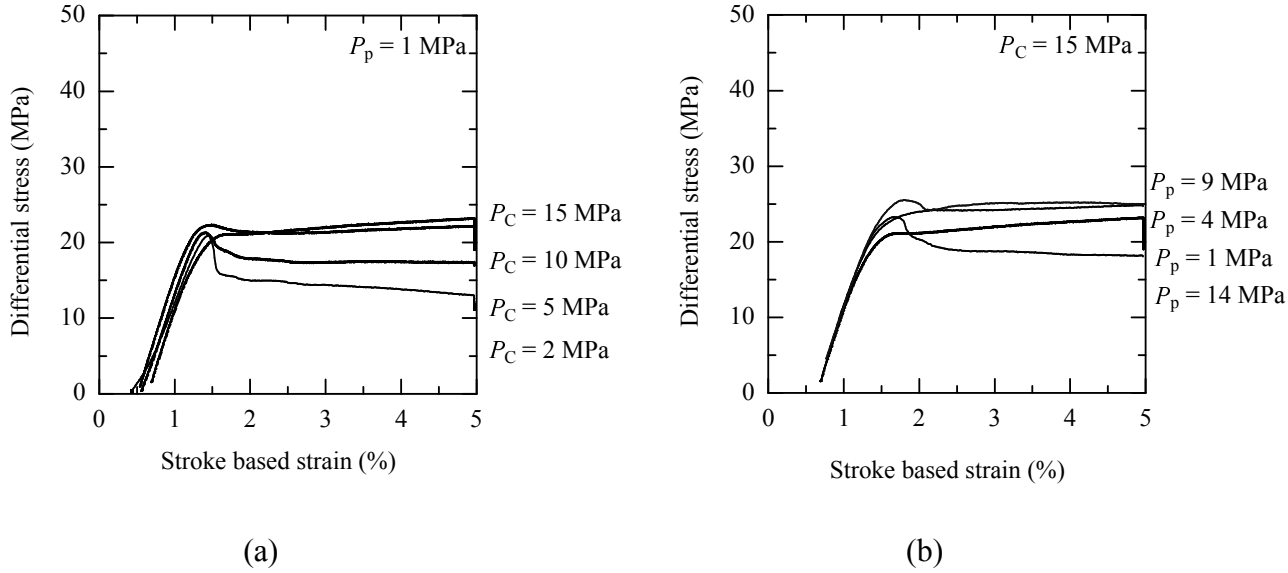


(a) (b)

Fig. 5.1 Differential stress versus stoke based strain for different confining pressures and pore pressures. (a) Effect of confining pressure (b) Effect of pore pressure.

With confining pressure of 15 MPa and with a pore pressure of 14 MPa, the rock exhibited strain-softening behavior, as shown in Fig. 5.1b. However, with pore pressures of 1 MPa, 4 MPa, and 9 MPa, it clearly exhibited a yield strength that increased with the pore pressure; with pore pressures of 1 MPa and 4 MPa, the rock did not exhibit a clear peak strength and exhibited strain hardening behavior.

*5.2.2 Micro- and macrostructures*

Microstructure analysis was conducted using the blue resin-impregnated thin-section images [Alam et al., 2014]. The thin section of the 15-MPa consolidated specimen was compared with that of the intact specimen to investigate the consolidation effect (Fig. 5.2a and b; blue spots represent pores). The porosity decreased by 41.23% (Fig. 5.2c) due to consolidation.

In the X-ray CT images [Alam et al., 2014] at $P_c$ = 1 MPa, a rupture plane was observed in the X−Z plane of the specimen after axial compression (Fig. 5.3). However, macroscopic fractures were not observed for the $P_c$ = 15 MPa case (Fig. 5.3b).

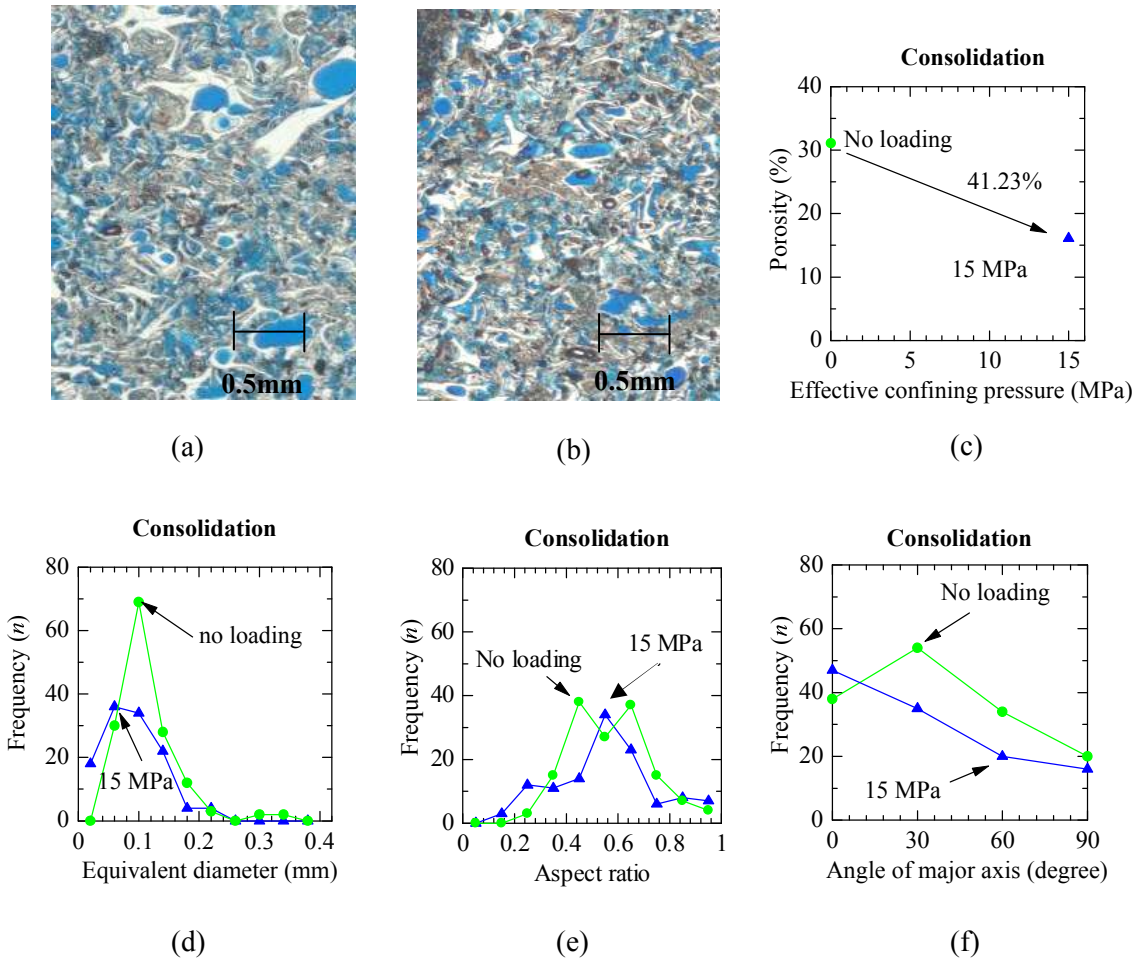


Fig. 5.2 Blue resin-impregnated thin-section images and analyses of the fresh and consolidated specimens of Shikotsu welded tuff. The blue spots represent pores in the rock. (a) Image of the intact specimen. (b) Image after consolidation at 15 MPa. (c) Porosity. (d) Equivalent diameter. (e) Aspect ratio. (f) Angle of major axis to the horizontal flow layer. [Alam et al., 2014, 2013]

An analysis of the pores around the rupture plane was performed using the blue resin-impregnated thin-section images of the specimens after axial compression at $P_c$ = 1 MPa. The porosity near the rupture plane increased by 16.99%, and was greater than that far from the rupture plane (Fig. 5.3f). The frequency value of $d_{pore}$ = 0.10 mm increased near the rupture plane (Fig. 5.3g), and the frequency value of $d_{pore}$ = 0.06 mm was dominant far from the rupture plane. The frequency of a pore aspect ratio of around 0.5 decreased near the rupture plane (Fig. 5.3h).

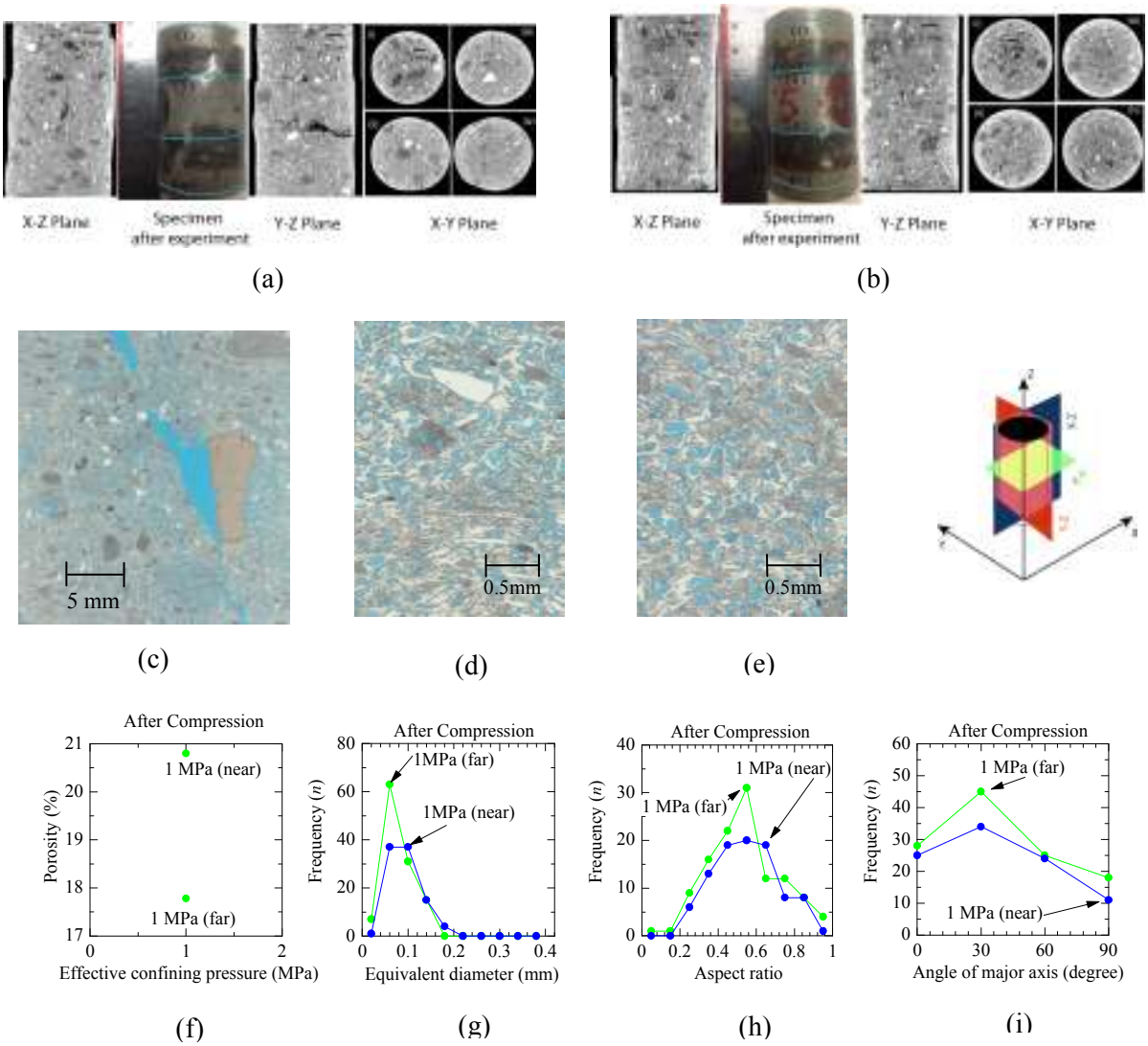


Fig. 5.3 Specimen, CT images, blue resin-impregnated thin-section images, and analyses after axial compression of Shikotsu welded tuff. Specimen and CT images at (a) 1 MPa and (b) 15 MPa. (c) Image at 1 MPa. Image at 1 MPa (d) near the shear plane and (e) far from the shear plane. (f) Porosity near and far from the rupture plane. (g) Equivalent diameter. (h) Aspect ratio. (i) Angle of major axis to the flow layer (horizontal). The loading direction is vertical. [Alam et al., 2014, 2013]

### *5.2.3 Effective stress coefficients*

#### *5.2.3.1 Effective stress coefficients by MFEM*

The MFEM could not be used to determine the effective stress coefficients for the peak strength in single stage or multistage triaxial tests, as shown in Fig. 5.4. In many cases, the strength with non-zero pore pressures was larger than that with zero pore pressure, as shown in Fig. 5.4c. This may be due to an end-cap like failure surface at higher stresses because of pore collapse [Zaman et al., 1994; Zimmerman et al., 1994],

due to crushing of the rock matrix, which consisted of volcanic glass. The decrease in $\alpha$ for residual strength with increasing effective confining pressure shows the progress of the pore collapse. Therefore, poroelasticity theory could not be applied to this condition.

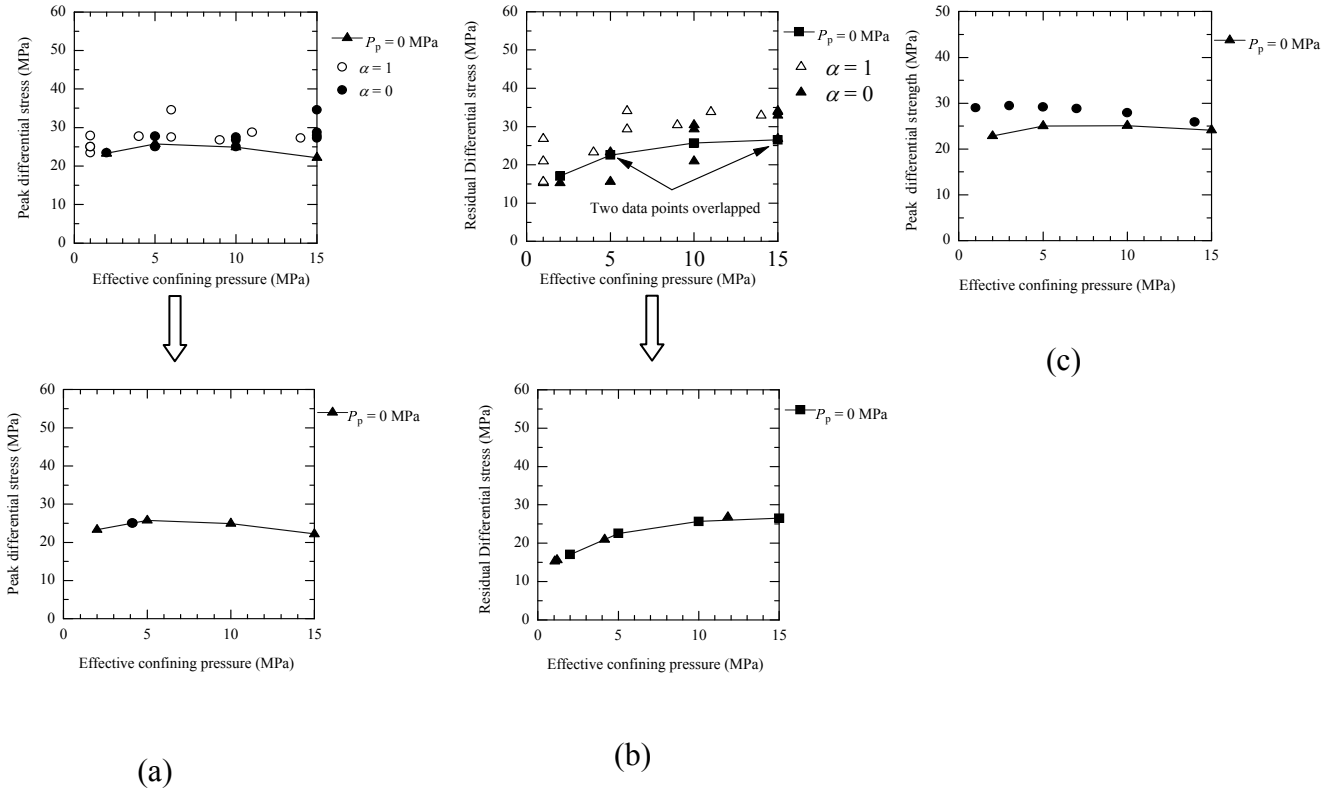


Fig. 5.4 (a) Peak differential stresses in single stage MFEM (b) Residual differential stresses in single stage MFEM and (c) Peak differential stresses of Shikotsu welded tuff by multi stage triaxial tests when $\alpha$ = 1.

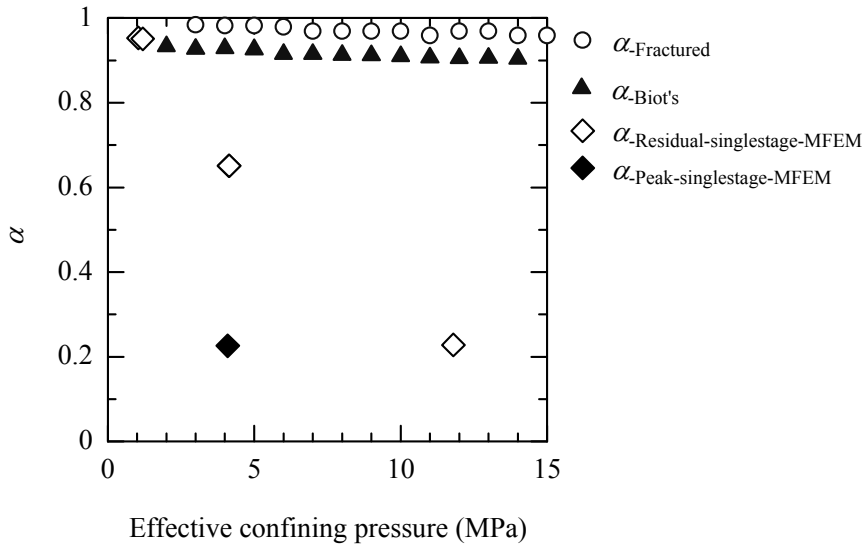


Fig. 5.5 Summary of effective stress coefficients

*5.2.3.2 Effective stress coefficients by Hydrostatic compression test*

In the drained hydrostatic compression tests with zero pore pressure, a nearly linear response of the volumetric strain was observed as a function of the hydrostatic pressure, as shown in Fig. 5.6. This was attributed to the microstructure of the rock, *i.e.*, there were few microcracks and a number of large circular pores that did not exhibit elastic closure (see Fig. 5.3).

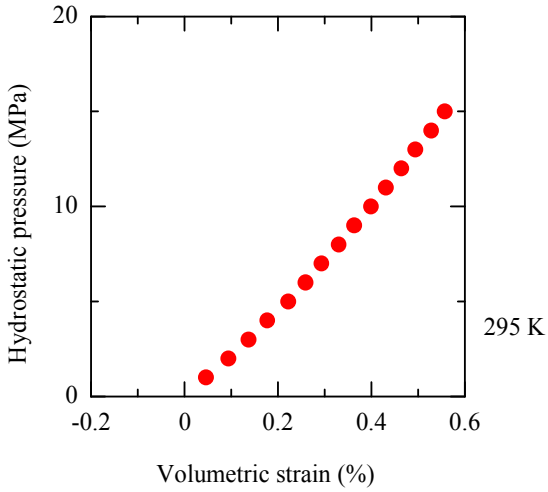


Fig. 5.6 Stress-strain curve in hydrostatic compression test for $P_p$=0

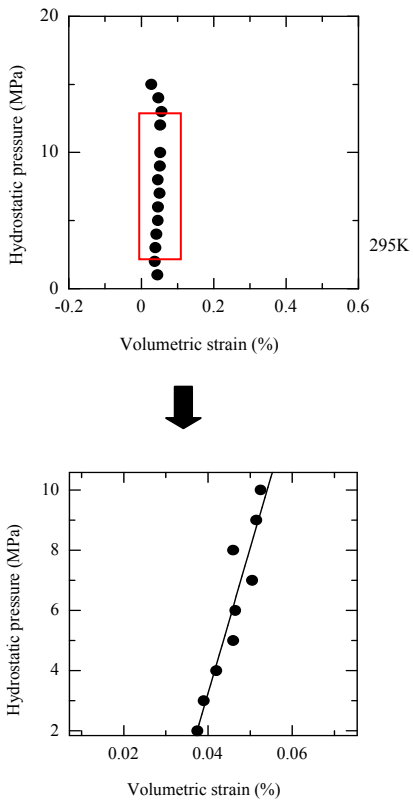


Fig. 5.7 Stress-strain curve in hydrostatic compression test with non zero pore pressure: $\Delta P_c = \Delta P_p$.

As a result, the bulk modulus was almost constant, and consequently, so was the effective stress coefficient, which was in the range 0.95 > $\alpha_{\text{-Biot's}}$ > 0.90, as shown in Fig. 5.5. The effective stress coefficients by the hydrostatic tests for fractured rock, $\alpha_{\text{-Fractured}}$ were larger than those for intact rock, and were close to unity, as shown in Fig. 5.5.

*5.2.3.3 General review of Effective stress coefficients for Shikotsu welded tuff*

The MFEM could not be used to determine the effective stress coefficients for the peak strength in single stage or multistage triaxial tests.

Assuming Eq. (2.8) for the effective stress coefficient, the constants *A* and *B* can be obtained for intact and fractured rocks.

Constant *A* and *B* for Eq.2.8 are shown in table 5.2.

Table 5.2 Constant *A* and *B* in Eq. 2.8 and Eq. 2.9

| Effective stress coefficients | A | B ($MPa^{-1}$) | coefficient of correlation \|r\| |
|---|---|---|---|
| Intact | 0.935 | 0.0024 | 0.96 |
| Fractured | 0.989 | 0.002 | 0.89 |

**5.3. Discussion**

*5.3.1 Applicability of the MFEM*

MFEM was not able to accurately apply for Shikotsu welded tuff to determine effective stress coefficients for the peak and residual strengths ($\alpha_{\text{-Peak}}$ and $\alpha_{\text{-Residual}}$).

*5.3.2 Relationship between the coefficient for intact rock and strengths*

As shown in Fig. 5.8, the model failed to describe the Shikotsu welded tuff. From the behavior at high normal stresses, it was apparent that pore collapse occurred, significantly changing the microstructure of the rock.

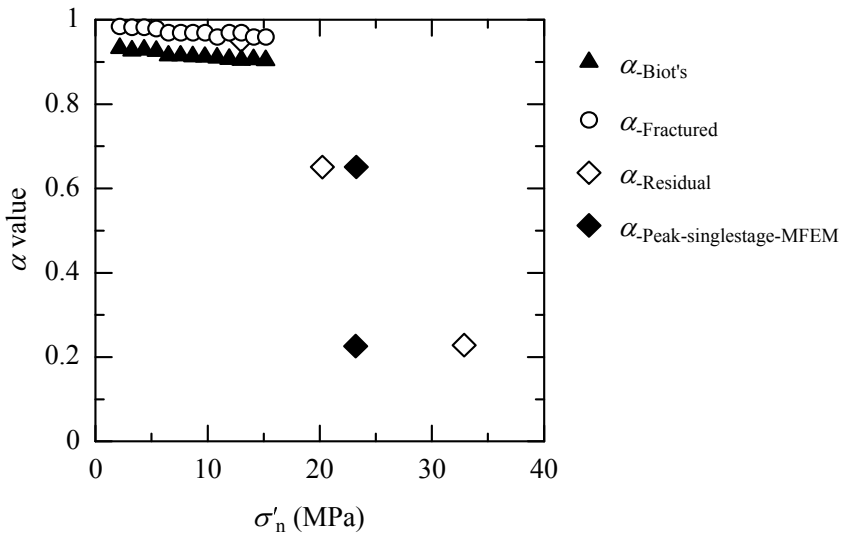


Fig. 5.8 Effective normal stress vs $\alpha$ relationship for Shikotsu welded tuff

# 6. Discussions

*6.1 Applicability of the MFEM*

MFEMs were successfully applied to Kimachi sandstone and Bibai sandstone for the determination of effective stress coefficient for the peak and residual strengths. However, only the multistage MFEM was applicable for Inada granite, since the rock was very brittle and the scatter in the strength was very large. Even the multistage MFEM was not able to accurately apply for Shikotsu welded tuff because of pore collapse. Based on these results, the multistage MFEM is recommended to obtain the effective stress coefficients for peak and residual strengths although the method cannot be applied for the rocks that undergo drastic structural change due, for example, to pore collapse. The strength correction in the multistage MFEM is particularly effective in obtaining results with a small amount of data scattering.

*6.2 Relationship between the coefficient for intact rock and for strengths*

The effective stress coefficients for Kimachi sandstone, both for peak and residual strengths and for the intact rock, can be well described using a linear fit, taking the effective normal stress on the rupture plane as the $x$-axis, as shown in Fig. 2.22 (assuming that the rupture plane is inclined by 30º). The coefficient values for peak and residual strengths for Bibai sandstone were also well approximated. Bibai sandstone contains few clay minerals. This would be the reason for very strong stress dependency of $\alpha_{\text{-Biot's}}$.

As shown in Fig. 4.7, the effective stress coefficient for Inada granite could not be accurately described using a linear fit. Allowing the scatter, however, a very rough estimation might be possible. The values for residual strength could not be obtained due to large scattering of the data; however, some mechanical analyses could be carried out assuming that the values lie on the linear fit.

As shown in Fig. 5.8, the model failed to describe Shikotsu welded tuff From the behavior of Shikotsu welded tuff, at high normal stresses, it was apparent that pore collapse occurred, significantly changing the microstructure of the rock.

*6.3 The choice of the effective stress coefficient*

For elastic stress analysis of such small structures in intact rock as boreholes, the coefficient for intact rock can be used, and the value of the coefficient can be evaluated using the results of the hydrostatic tests for intact rock, as well as a number of conventional methods.

To evaluate rock failure, however, the coefficient for the peak strength should be used. This coefficient can be evaluated using the multistage MFEM, except for rocks that undergo drastic structural change due,

for example, to pore collapse. The coefficient for the peak strength was considerably smaller than that for intact rock. Combining the coefficients for intact rock and the peak strength via an effective normal stress may allow a seamless analysis. This can be done only for Kimachi sandstone though.

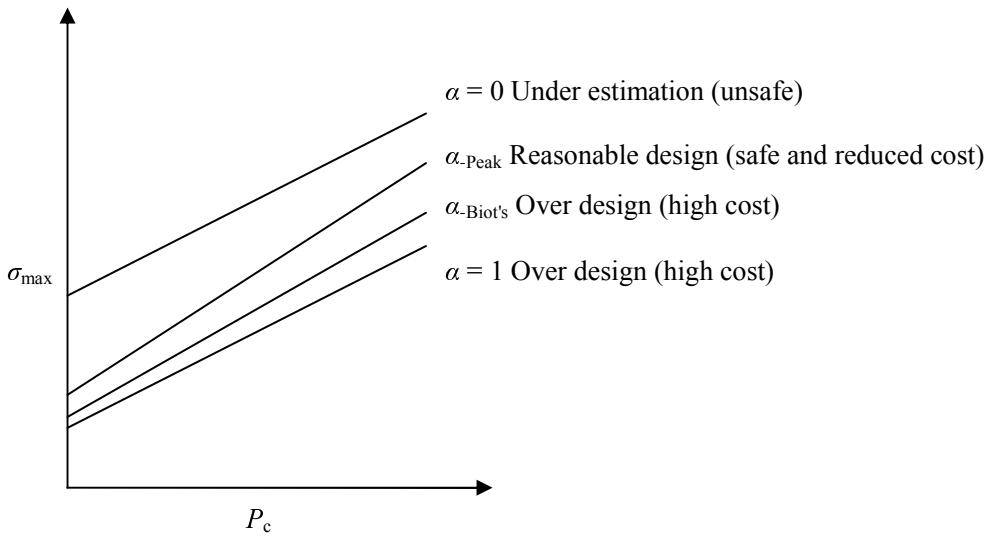


Fig.6.1 Schematic diagram showing peak stress estimation based on different effective strength coefficients.

If Terzaghi's effective stress coefficient ($\alpha$ = 1) is used in failure evaluations of rock, the effective strength of rock will be under-estimated (Fig. 6.1). In the case of $\alpha_{\text{-Biot's}}$ which is greater than $\alpha_{\text{-Peak}}$ for Kimachi sandstone, still the effective strength of rock will be underestimated. This leads overdesign. If effective stress coefficient is assumed as zero, the effect of pore pressure to the effective stress is totally ignored and the structure is in danger under such conditions. However, if the effective stress coefficient for peak strength; $\alpha_{\text{-Peak}}$ as evaluated in this research is used, the exact effective strength can be evaluated, thereby saving cost for the excavations ensuring safety which is reasonable than other two occasions.

For the elastic stress analysis of a structure in a rock mass, the coefficient for fractured rock can be used since rock maasses are fractured; though, there exists a problem due to differences in the scale and the origin between rupture planes in fractured rock specimens and fractures in a rock mass. The coefficient can be evaluated using hydrostatic tests for fractured rock; however, in practice, this test can be skipped because the coefficient is larger than that of intact rock, and is close to unity.

The coefficient for the residual strength should be used to evaluate rock mass failure. This coefficient can be evaluated using the multi-stage MFEM. However, the evaluation of this coefficient was successful only for sandstones (Kimachi sandstone and Bibai sandstone) and was found to to be almost same as the coefficient for intact rock, $\alpha_{\text{-Biot's}}$. Further investigation into the coefficient for the residual strength is required.

# 7. Concluding remarks

To determine the effective stress coefficient for peak and residual strengths ($\alpha_{\text{-Peak}}$ and $\alpha_{\text{-Residual}}$) of rocks, Modified Failure Envelope Method (MFEM) was proposed incorporating the results of both single stage and multistage triaxial compression tests based on the failure envelope. Multistage triaxial tests are used to reduce the number of specimens as well as the error caused by differences in the mechanical properties between specimens. The effective stress coefficients for intact and fractured rock ($\alpha_{\text{-Biot's}}$ and $\alpha_{\text{-Fractured}}$) were also evaluated using conventional methods, and the data were compared with the coefficient values obtained by MFEM for the peak and residual strengths.

The types of rock considered were Kimachi sandstone as a medium-hard clastic rock, Bibai sandstone as a hard clastic rock, Inada granite as a hard crystalline rock and Shikotsu welded tuff as a soft pyroclastic rock, to cover wide range of physical properties of rock under confining pressures of 1-15 MPa at 295 K.

Base on the results of rock types, an equation to obtain the effective stress coefficient from total confining pressure and pore pressure, and a method to choose the coefficients for elastic stress analyses and failure evaluations for intact rock structures or structures in rock mass were also proposed.

Main findings of effective stress coefficient are as follows.

(i) Kimachi sandstone

In the drained hydrostatic compression test the effective stress coefficient for intact rock, $\alpha_{\text{-Biot's}}$ decreased with increasing confining pressure, and was in the range $1 > \alpha_{\text{-Biot's}} > 0.8$. The effective stress coefficients by hydrostatic tests for fractured rock, $\alpha_{\text{-Fractured}}$ were larger than those for intact rock $\alpha_{\text{-Biot's}}$ and were close to unity.

The most reliable effective stress coefficients by multistage MFEM for the peak strength, $\alpha_{\text{-Peak}}$ decreased with increasing effective confining pressure and was in the range $0.8 > \alpha_{\text{-Peak}} > 0.4$.

For residual strength, the most reliable $\alpha_{\text{-Residual}}$ by multistage MFEM ascending $P_c$ approach was almost same as $\alpha_{\text{-Biot's}}$.

(ii) Bibai sandstone

In the drained hydrostatic compression test the effective stress coefficient for intact rock, $\alpha_{\text{-Biot's}}$ decreased with increasing confining pressure, and was in the range $1 > \alpha_{\text{-Biot's}} > 0.5$. The effective stress coefficients for fractured rock, $\alpha_{\text{-Fractured}}$ were close to unity.

The effective stress coefficients for the peak strength, $\alpha_{\text{-Peak}}$ by multistage MFEM decreased with increasing effective confining pressure and was in the range $0.9 > \alpha_{\text{-Peak}} > 0.4$.

For residual strength, $\alpha_{\text{-Residual}}$ by multistage MFEM ascending $P_c$ was almost same as $\alpha_{\text{-Biot's.}}$

(iii) Inada granite

In the drained hydrostatic compression tests, the effective stress coefficient for intact rock, $\alpha_{\text{-Biot's}}$ decreased with increasing confining pressure and was in the range $0.9 > \alpha_{\text{-Biot's}} > 0.7$. The effective stress coefficients for fractured rock, $\alpha_{\text{-Fractured}}$ were close to unity.

The effective stress coefficient for peak strength by multistage MFEM decreased with effective confining pressure and were in the range $0.8 > \alpha_{\text{peak}} > 0.2$. $\alpha$ for residual strength by multistage triaxial tests were not carried out.

(iv) Shikotsu welded tuff

The effective stress coefficient for intact rock, $\alpha_{\text{-Biot's}}$ slightly decreased with increasing confining pressure and was in the range $0.95 > \alpha_{\text{-Biot's}} > 0.90$. The effective stress coefficients for fractured rock, $\alpha_{\text{-Fractured}}$ were close to unity.

The MFEM could not be used to determine the effective stress coefficients for the peak strength in single stage or multistage triaxial tests. In many cases, the strength with non-zero pore pressures was larger than that with zero pore pressure. This may be due to an end-cap like failure surface at higher stresses because of pore collapse due to crushing of the rock matrix, which consisted of volcanic glass. Poroelasticity theory could not be applied to this condition.

$\alpha_{\text{-Biot's}}$ can be used to evaluate stress distribution of small rock structures and can be obtained by any of the conventional methods. $\alpha_{\text{peak}}$ would be required to evaluate failure of the rock around the structures and it can be obtained by multistage MFEM. $\alpha_{\text{-Fractured}}$ can be used to evaluate stress distribution of large rock structures and can be assumed to be unity. $\alpha_{\text{-Residual}}$, however would be required to evaluate failure of the structures and can be obtained by multistage MFEM ascending $P_c$ approach.

Choosing the suitable $\alpha$ can make design of rock structure safer with reducing cost. Further investigations are required for $\alpha_{\text{-Residual}}$ because it was obtained only for the sandstones. I would be very happy if these findings contribute reasonable design of rock structures.

**References**


Alam, A.K.M. B., Niioka, M., Fujii Y., Fukuda, D., Kodama, J. (2014), Effect of confining pressure on the permeability of three rock types under compression, Int J of Rock Mech Min Sci Vol. 65(1), pp. 49-61.

Alam, A.K.M.B., Niioka, M., Fukuda, D. and Fujii, Y. (2013), Confining Pressure Effect on Structual Changes in Rock Types under Consolidation and Compression, Proc. MMIJ Fall Meeting, , PY-7, 3 September, Sapporo, Hokkaido University.

Alam, M. M., Borre, M. K., Fabricius, I. L., Hedegaard, K., Røgen, B., Hossain, Z., Krogsbøll, A. S., (2010). Biot's coefficient as an indicator of strength and porosity reduction: calcareous sediments from Kerguelen Plateau. Journal of Petroleum Science and Engineering Vol. 70, pp. 282–297

Biot, M. A., (1941). General theory of three dimentional consolidation, J Appl Phys; Vol. 12(2), pp. 155–164.

Biot, M. A., (1955). Theory of elasticity and consolidation for a porous anisotropic solid. J Appl Phys; Vol. 26, pp 182–185.

Biot, M. A., Willis, D. G., (1957). The elastic coefficients of the theory of consolidation. ASME J Appl Mechs, Vol. 24, pp. 594–601.

Dassanayake, A. and Fujii, Y. (2013), Evaluation of Biot's Effective Stress Constant for Peak and Residual Strengths for Shikotsu Welded Tuff and Kimachi Sandstone by using Modified Failure Envelope Method, Proc. MMIJ Fall Meeting 2013 Sapporo, PY-6, p. 570, Hokkaido University, Sapporo, Sep. 3.

Dassanayake, A. B. N. and Fujii, Y. (2014a), Biot's Effective Stress Coefficient of Rocks for Peak and Residual Strengths by Modified Failure Envelope Method, in Alejiano, L. et al. (eds.), Rock Engineering and Rock Machanics: Structures in and on Rock Masses (Proc. EUROCK 2014), pp. 155-160, Vigo, Spain, May. 27.

Dassanayake, A. B. N., Fujii, Y., Fukuda, D. and Kodama, J. (2014b), Significant Differences in Effective Stress Coefficient for Rocks within Elastic Region and Peak and Residual Strengths, Proc. ARMS8 (2014 ISRM International Symposium - 8th Asian Rock Mechanics Symposium), RP1-4, Sapporo, Japan, Oct. 14, 2014.

Dassanayake, A.B.N., Fujii, Y., Fukuda, D. and Kodama, J. (2015), A New Approach to Evaluate Effective Stress Coefficient for Strength in Kimachi Sandstone, J. Petrol. Sci. Engng., Vol. 131, pp. 70-79

Detournay E., Cheng A. H-D., (1993). Fundamentals of poroelasticity. In: Hudson JA, editor. Comprehensive rock engineering. Oxford: Pergamum, pp. 113-171.

Dhakal G., Yoneda T., Kato M., Kaneko K. (2002). Slake durability and mineralogical properties of some pyroclastic and sedimentary rocks. Eng geol; Vol. 65, pp. 31−45.

Fjear, E., Holt R. M., Horsrud, P. (2008). Petroleum Related Rock Mechanics 2nd ed. Amsterdam, Boston: Elsevier, pp. 66-70.

Franquet, J. A., Abass, H. H., (1999). Experimental evaluation of Biot's poroelastic parameter - Three different methods. 37th U.S. Symposium on Rock Mechanics (USRMS), June 7-9 Vail, CO, Balkema, Rotterdam, .pp. 349–355.

Fukuda, D., Nara, Y., Kobayashi, Y., Maruyama, M., Koketsu, M., Hayashi, D., Ogawa, H., Kaneko, K. (2012), Investigation of self-sealing in high-strength and ultra-low-permeability concrete in water using micro-focus X-ray CT, Cement and Concrete Research, Vol. 42, pp. 1494-1500.

Geertsma, J., (1957). The effect of fluid pressure decline on volumetric changes of porous rocks. Petroleum Transactions, AIME, Vol. 210, pp. 331–340.

Hu, D.W., Zhou, H., Zhang, F., Shao, J.F., (2010). Evolution of poroelastic properties and permeability in damaged sandstone. Int J Rock Mech Min Sci; Vol. 47, pp. 962–973.

Kovari, K., Tisa, A., Einstein, H.H., Franklin, J.A., (1983). Suggested methods for determining the strength of rock materials in triaxial compression: revised version. Int J Rock Mech Min Sci; Vol. 206, pp. 283–90.

Makhnenko, R.M., Labuz, J.F., (2013). Unjacketed bulk compressibility of sandstone in laboratory experiments. Proceedings of the 5th BIOT Conference on Poromechanics, Vienna, Austria, 10-12 July 2013, paper No. 304.

Mese, A., Tutuncu, A.N., (2000). A novel experimental technique for investigation of pore pressure effect on acoustic and mechanical properties in unconsolidated shaly sands and shales. Pacific Rocks 2000: Rock Around the Rim, proceedings of the 4th North American Rock Mechanics Symposium Seattle, Washington, July 31–August 3, 2000, pp. 173–179.

Nur, A., Byerlee, J. D., (1971). An exact effective stress law for elastic deformation of rock with fluids. Journal of Geophysical Research Solid Earth, Vol. 76, pp. 6414–6419.

Schindelin, J., Arganda-Carreras, I., Frise, E. et al. (2012), "Fiji: an open-source platform for biological-image analysis", *Nature methods* **9(7)**, pp. 676-682, PMID 22743772.

Schneider, C. A.; Rasband, W. S. & Eliceiri, K. W. (2012), "NIH Image to ImageJ: 25 years of image analysis", *Nature methods* **9(7)**, pp. 671-675,PMID 22930834.

Sheng, Q. Y., Hong,W. J., Shan,Y. W. (2012). Experimental Investigation on the Strength, Deformability, Failure Behavior and Acoustic Emission Locations of Red Sandstone Under Triaxial Compression. Rock Mechanics and Rock Engineering, vol. 45, no. 4, pp. 583–606.

Terzaghi, K., (1936). The shearing resistance of saturated soils and the angle between the planes of shear. First Int. Conf. Soil Mech., Vol. 1, Harvard Univ., Cambridge, Mass.:54-56.

Youn, H., Tonon, F., (2010). Multi-stage triaxial test on brittle rock. Int J Rock Mech Min Sci; Vol. 47, pp. 678–684.

Zaman M, Roegiers JC, Abdulraheem A, Azeemuddin M. (1994). Pore collapse behaviour of weakly cemented and porous rocks. J Energy Resourc Tech; Vol. 116, pp. 97–103.

Zhang, K., Zhou, H., Hu, D., Zhao, Y., Feng, X., (2009). Theoretical model of effective stress coefficient for rock/soil-like porous materials. Acta Mechanica Solida Sinica Vol. 22, pp. 251–260.

Zimmerman R.W., Myer L.R., Cook N.G.W., (1994). Grain and void compression in fractured and porous rocks. Int J Rock Mech Min Sci;Vol. 31, pp. 179–84.

Zimmerman, R.W., (1991). Compressibility of Sandstones. Elsevier, New York. p.173.